Large Displacement Analysis of Sandwich Plates and Shells with Symmetric/Asymmetric Lamination

Y. Liang[1] and B.A. Izzuddin[2]

Abstract

This paper proposes a kinematic model for sandwich plates and shells, utilising a novel zigzag function that is effective for symmetric and asymmetric cross-sections, and employing a piecewise through-thickness distribution of the transverse shear strain. The proposed model is extended to large displacement analysis using a co-rotational framework, where a 2D local shell system is proposed for the direct coupling of additional zigzag parameters. A 9-noded co-rotational shell element is developed based on the proposed approach, which utilises the MITC method for overcoming locking effects. Several linear/nonlinear analysis examples of sandwich structures demonstrate the effectiveness of the proposed approach.

Keywords: sandwich plates; sandwich shells; soft core; zigzag; transverse shear strain; large displacement.

[1] Research student, Department of Civil and Environmental Engineering, Imperial College London SW7 2AZ.
[2] Professor of Computational Structural Mechanics, Department of Civil and Environmental Engineering, Imperial College London, SW7 2AZ, (Corresponding author, b.izzuddin@imperial.ac.uk).

1 INTRODUCTION

Sandwich structures consisting of two stiff outer layers bonded to a soft core have been widely adopted in many engineering applications. Due to the large face-to-core stiffness ratio, such structures are characterised by a zigzag form of displacements. The classical lamination theory (CLT) and the first-order shear deformation theory (FSDT) [1], representing extensions of the Kirchhoff and Reissner-Mindlin plate theories to the laminate, cannot accurately predict the response of sandwich structures due to the assumption of linear variation in displacement over the thickness. Higher-order shear deformation theories (HSDTs) [2-3] improve the accuracy of the global response by introducing additional variables with higher-order out-of-plane z expansions of the displacement fields, but these z expansions, which are defined at the multi-layer level, cannot describe the discontinuity associated with the variation of mechanical properties through the thickness.

There are two main approaches that include the zigzag effect into 2D modelling: layer-wise (LW) description and equivalent single layer (ESL) description with the inclusion of Murakami's zigzag function [4]. LW models [5-7] regard each layer as an independent plate or shell, and employ any of the CLT, FSDT and HSDTs at the layer level. The compatibility conditions are satisfied by imposing displacement constraints at laminar interfaces. Nevertheless, the number of displacement variables in LW models depends on the number of constitutive layers, though the number of displacement fields can be reduced by also enforcing the continuity of transverse stresses at laminar interfaces [8-14]. These methods are typically labelled as zigzag theories.

The ESL description considers the zigzag effect with relative ease, where a piecewise linear zigzag function, such as the one first proposed by Murakami [10], is added to the FSDT and HSDTs [11-12]. Approaches in this category are denoted as 'EDZ' models (where 'E' stands for the ESL description, 'D' stands for the employment of principle of virtual displacements, and 'Z' indicates the inclusion of a zigzag function) [11]. The EDZ models improve the results of FSDT and HSDTs with relative ease, and the degrees of freedom (DOFs) of EDZ models are independent of the number of layers. On the basis of the EDZ

models, a group of mixed formulations have also been developed, denoted as 'EMZC' models (where 'M' stands for the mixed formulation, and 'C' means the fulfilment of inter-laminar continuity) [11], where continuous transverse shear and normal stresses are assumed and Reissner's variational principle is employed, thereby achieving the continuity of both displacements and transverse stresses. The EDZ and EMZC models have been widely used in the analysis of thin-to-thick laminations as well as sandwich structures [11-15]. It is noted, however, that the effectiveness of the EDZ and EMZC models relies on the effectiveness of Murakami's zigzag function (MZZF), which depends further on the material properties and thickness of each constitutive layer as well as the stacking sequence. In plate bending problems associated with an asymmetrically laminated sandwich plate [15], it has been shown that higher-order z expansions of displacements are required for the EDZ models to achieve sufficient accuracy owing to the ineffectiveness of the MZZF, while Carrera [16] suggested that that the effectiveness of the MZZF may be improved with the employment of the mixed assumption. Nevertheless, the ESL models with the inclusion of MZZF provide a convenient approach for considering the lamination effects in terms of accuracy versus the required computational effort, and these models have also been employed in finite element formulations to analyse sandwich and lamination problems involving geometric nonlinearity [17-20].

Motivated by Murakami's work [10], this paper proposes an efficient three-layered model for the analysis of sandwich plates and shells. While similar in principle to the EDZ model, an important difference is the introduction of a novel zigzag function over the full plate thickness that is specific to sandwich plates/shells with a soft core. This enriches the classical Reissner-Mindlin formulation [21-22] by allowing for cross-sectional warping, and satisfies the continuity of displacements at laminar-interfaces a priori via the assumed zigzag mode. The proposed zigzag function is shown to provide good accuracy for both symmetric and asymmetric lay-ups, while achieving computational efficiency through the use of a minimal number of additional zigzag displacement fields. On the other hand, a piecewise linear-constant-linear distribution is assumed for the transverse shear strain, which imposes no

constraints on transverse shear stresses but is shown to provide an accurate representation of the actual distribution without sacrificing computational efficiency.

In formulating large displacement 2D shell elements for small strain problems, the relationship between the strain and displacement fields is highly nonlinear and complex if the displacement fields are referred to a fixed coordinate system, such as in the Total Lagrangian approach [23-24], where the nonlinear strain terms arise mainly from the element rigid body rotations. Instead, the co-rotational approach, which decomposes the element motion into rigid body and strain-inducing parts via the use of a local co-rotational system, allows the employment of low-order, even linear, relationships between the strain and local displacement fields [25]. In this respect, the co-rotational approach shifts the focus of geometric nonlinearity from the continuum level to the discrete nodal level, and it can act as a standard harness around different local element formulations [26], upgrading such formulations to large displacement analysis with relative ease. In addition, when laminations are considered, the co-rotational system provides a reference orientation for the definition of the zigzag displacement variables which are associated with local cross-sectional warping only. In this context, co-rotational transformations of the zigzag displacement variables are avoided in this work through the introduction of a 2D 'shell' coordinate system, which follows the local co-rotational element system, thus achieving significant computational benefits. Further benefits arise in the local element formulation with the definition of a 2D 'shell' coordinate system that is continuous over the shell structure, where three such definitions are proposed in this paper. Notwithstanding the above benefits, it is important to note that the co-rotational approach offers no particular benefits in large strain problems, for which a Total Lagrangian approach would be more suited [24].

The application of the proposed sandwich shell model is illustrated for a 9-noded shell element [27-28], which employs a bisector co-rotational system [25] for modelling geometric nonlinearity. The basic local displacement variables consistent with the Reissner-Mindlin formulation are related to the global variables according to discrete nonlinear co-rotational transformations, while the additional zigzag displacement variables are defined directly in the 2D curvilinear shell system. Furthermore, in order to alleviate membrane and shear locking

which arise with conforming displacement-based shell elements, an assumed strain approach is considered. Amongst the different assumed strain methods, the Mixed Interpolation Tensorial Components (MITC) method [29-30] is widely used to overcome locking, offering a two-level approximation that samples and interpolates strain components in a covariant coordinate system at a selection of positions. The application of the MITC method to a 9-noded shell element has been shown to yield a much improved element performance [31-33], thus the MITC approach is utilised herein for each constitutive layer of the 9-noded shell element to overcome locking.

The paper proceeds with presenting the proposed kinematic description for sandwich shells, the effectiveness of which is then demonstrate with reference to a 1D linear problem. The enhancements required for large displacement analysis of shells are subsequently presented, and the application of the proposed sandwich shell model is illustrated for a 9-noded co-rotational shell element. Several linear and nonlinear numerical examples are finally presented to demonstrate the accuracy and efficiency of the proposed approach for the analysis of sandwich shell structures with both symmetric and asymmetric lay-ups.

2 KINEMATIC DESCRIPTION FOR SANDWICH SHELLS

A kinematic model is proposed in this section for sandwich shells, with specific reference to the through-thickness variation of displacement fields and the transverse shear strains. Figure 1 depicts the sandwich model for a plate along with the local coordinates, where the x- and y-axes are located at the middle surface while the z-axis is normal to the plate, and where each layer is identified by a unique index. It is important to note that while the kinematic descriptions is initially presented for a plate problem, it is equally applicable to local formulations of shallow shells, as elaborate in Section 2.2. Furthermore, through incorporation within a co-rotational framework, it is also applicable to the nonlinear analysis of general curved shells, as presented in Section 4 and demonstrated by the numerical examples of Section 6.

2.1 Geometry and Displacement Fields

In this sandwich plate model, a piecewise linear variation of planar displacements in the z direction is assumed, thus readily satisfying C^0-continuity at laminar interfaces. Accordingly, the through-thickness distribution of the planar displacements can be decomposed into four independent displacement modes $\Lambda_i(z)(i=1\rightarrow 4)$ (Figure 2), including a constant and a linear mode, Λ_1 and Λ_2, in accordance with the Reissner-Mindlin kinematic hypothesis, as well as two zigzag modes, Λ_3 and Λ_4, accounting for the zigzag effect. Λ_3 and Λ_4 are both orthogonal to the constant and linear modes while associated with respectively different and identical rotations of the normal in the two face sheets; these are expressed as:

$$\Lambda_3(z)=\begin{cases}\hat{a}_3^{(1)}z+\hat{b}_3^{(1)} & z\in\left[h_{1-},h_{1+}\right]\\ \hat{a}_3^{(2)}z+\hat{b}_3^{(2)} & z\in\left[h_{2-},h_{2+}\right]\\ \hat{a}_3^{(3)}z+\hat{b}_3^{(3)} & z\in\left[h_{3-},h_{3+}\right]\end{cases} \tag{1}$$

$$\Lambda_4(z)=\begin{cases}\hat{a}_4^{(1)}z+\hat{b}_4^{(1)} & z\in\left[h_{1-},h_{1+}\right]\\ \hat{a}_4^{(2)}z+\hat{b}_4^{(2)} & z\in\left[h_{2-},h_{2+}\right]\\ \hat{a}_4^{(3)}z+\hat{b}_4^{(3)} & z\in\left[h_{3-},h_{3+}\right]\end{cases} \tag{2}$$

in which h_- and h_+ denote the values of z at the bottom and top of the cross-section, respectively; h_{k-} and h_{k+} refer to the values of z at the bottom and top of layer (k), respectively; and expressions of $\hat{a}_i^{(k)}$ and $\hat{b}_i^{(k)}$ (i=3,4) are provided in Appendix A.

The variation of planar displacements under bending is investigated by performing a 2D plane-stress analysis of a sandwich beam with a soft core, which indicates that the two stiff layers have almost identical rotations of their respective normals, whereas the core can have a different rotation. Therefore, following on from the observed cross-sectional behaviour, the contribution from Λ_3 is neglected, and $\Lambda_4(z)$ is proposed as a zigzag function specific to sandwich structures, applicable regardless of cross-sectional symmetry, which is re-denoted as $\Lambda(z)\equiv\Lambda_4(z)$.

It is important to note that for symmetrically laminated sandwich structures the zigzag function $\Lambda(z)$ is equivalent to Murakami's zigzag function (MZZF), which is defined as [10]:

$$f(z)=(-1)^k\zeta^{(k)},\quad \zeta^{(k)}=\frac{2(z-z^{(k)})}{h_k}\quad z\in\left[h_{k-},h_{k+}\right] \tag{3}$$

where h_k is the thickness of layer (k), and $z^{(k)}$ is the extracted value of z on the middle surface of layer (k).

However, if the sandwich plate is asymmetrically laminated, $\Lambda(z)$ is more effective than the MZZF, as will be illustrated in Section 3.

The addition of the zigzag function to the Reissner-Mindlin planar displacements yields the following planar displacements:

$$u_\alpha(x,y,z) = u_{\alpha 0}(x,y) + z\theta_\alpha(x,y) + \Lambda(z)\vartheta_\alpha(x,y) \quad (\alpha = x,y) \tag{4}$$

where $u_{\alpha 0}$ are the planar displacement fields along the x- or y-axis evaluated on the middle surface; θ_α are the components of the normal vector along the x- or y-axis in the absence of zigzag displacements; ϑ_α are the additional fields associated with the proposed zigzag function along the x- or y-axis. The transverse displacement is assumed to be constant through the plate thickness, and is thus denoted by $u_{z0}(x,y)$.

2.2 Kinematics of individual layer

Each constitutive layer of the sandwich model is regarded as a pseudo plate. At layer (k) ($k = 1 \to 3$), the translational displacements on its middle surface are obtained as:

$$u_\alpha^{(k)} = u_{\alpha 0} + z^{(k)}\theta_\alpha + \Lambda^{(k)}\vartheta_\alpha \quad (\alpha = x,y) \tag{5a}$$

$$u_z^{(k)} = u_{z0} \tag{5b}$$

where $\Lambda^{(k)} \equiv \Lambda(z^{(k)})$ represents the extracted value of the zigzag function $\Lambda(z)$ on the middle surface of layer (k); $z^{(k)}$ is the extracted value of z on the middle surface of layer (k). The rotational displacements of layer (k) are derived by taking the first derivatives of the planar displacements with respect to z:

$$\theta_\alpha^{(k)} = \left.\frac{\partial u_\alpha}{\partial z}\right|_{z^{(k)}} = \theta_\alpha + \lambda^{(k)}\vartheta_\alpha, \quad \lambda^{(k)} = \left.\frac{\partial \Lambda}{\partial z}\right|_{z^{(k)}} \quad (\alpha = x,y) \tag{6}$$

Accordingly, the following relationship holds at each layer:

$$\mathbf{u}^{(k)} = \mathbf{T}_c^{(k)}\mathbf{u}_c + \mathbf{T}_a^{(k)}\mathbf{u}_a \tag{7}$$

$$\mathbf{T}_c^{(k)} = \begin{bmatrix} 1 & 0 & 0 & z^{(k)} & 0 \\ 0 & 1 & 0 & 0 & z^{(k)} \\ 0 & 0 & 1 & 0 & 0 \\ 0 & 0 & 0 & 1 & 0 \\ 0 & 0 & 0 & 0 & 1 \end{bmatrix} \tag{8a}$$

$$\mathbf{T}_a^{(k)} = \begin{bmatrix} \Lambda^{(k)} & 0 \\ 0 & \Lambda^{(k)} \\ 0 & 0 \\ \lambda^{(k)} & 0 \\ 0 & \lambda^{(k)} \end{bmatrix} \tag{8b}$$

where $\mathbf{u}_c = \left\langle u_{x0}, u_{y0}, u_{z0}, \theta_x, \theta_y \right\rangle^T$ are the basic local displacement fields consistent with the Reissner-Mindlin formulation; $\mathbf{u}_a = \left\langle \vartheta_x, \vartheta_y \right\rangle^T$ are the additional displacement fields associated with the zigzag function $\Lambda(z)$; and $\mathbf{u}^{(k)} = \left\langle u_x^{(k)}, u_y^{(k)}, u_z^{(k)}, \theta_x^{(k)}, \theta_y^{(k)} \right\rangle^T$ are the displacement fields at layer (k).

The strain state within each layer (k) is fully determined by the membrane strains $\boldsymbol{\varepsilon}_m^{(k)}$, bending generalised strains $\boldsymbol{\varepsilon}_b^{(k)}$, and transverse shear strains $\boldsymbol{\varepsilon}_s^{(k)}$. The various generalised strains are obtained as follows:

$$\boldsymbol{\varepsilon}_m^{(k)} = \begin{Bmatrix} \varepsilon_x^{(k)} \\ \varepsilon_y^{(k)} \\ \gamma_{xy}^{(k)} \end{Bmatrix} = \begin{Bmatrix} \dfrac{\partial u_x^{(k)}}{\partial x} \\ \dfrac{\partial u_y^{(k)}}{\partial y} \\ \dfrac{\partial u_x^{(k)}}{\partial y} + \dfrac{\partial u_y^{(k)}}{\partial x} \end{Bmatrix} + \begin{Bmatrix} \dfrac{1}{2}\left(\dfrac{\partial z_0}{\partial x} + \dfrac{\partial u_z^{(k)}}{\partial x} \right)^2 - \dfrac{1}{2}\left(\dfrac{\partial z_0}{\partial x} \right)^2 \\ \dfrac{1}{2}\left(\dfrac{\partial z_0}{\partial y} + \dfrac{\partial u_z^{(k)}}{\partial y} \right)^2 - \dfrac{1}{2}\left(\dfrac{\partial z_0}{\partial y} \right)^2 \\ \left(\dfrac{\partial z_0}{\partial x} + \dfrac{\partial u_z^{(k)}}{\partial x} \right)\left(\dfrac{\partial z_0}{\partial y} + \dfrac{\partial u_z^{(k)}}{\partial y} \right) - \left(\dfrac{\partial z_0}{\partial x} \right)\left(\dfrac{\partial z_0}{\partial y} \right) \end{Bmatrix} \tag{9a}$$

$$\boldsymbol{\varepsilon}_b^{(k)} = \begin{Bmatrix} \kappa_x^{(k)} \\ \kappa_y^{(k)} \\ \kappa_{xy}^{(k)} \end{Bmatrix} = \begin{Bmatrix} \dfrac{\partial \theta_x^{(k)}}{\partial x} \\ \dfrac{\partial \theta_y^{(k)}}{\partial y} \\ \dfrac{\partial \theta_x^{(k)}}{\partial y} + \dfrac{\partial \theta_y^{(k)}}{\partial x} \end{Bmatrix} \tag{9b}$$

$$\boldsymbol{\varepsilon}_s^{(k)} = \begin{Bmatrix} \gamma_{xz}^{(k)} \\ \gamma_{yz}^{(k)} \end{Bmatrix} = \begin{Bmatrix} \theta_x^{(k)} + \dfrac{\partial u_z^{(k)}}{\partial x} \\ \theta_y^{(k)} + \dfrac{\partial u_z^{(k)}}{\partial y} \end{Bmatrix} \tag{9c}$$

in which z_0 represents the offset of the shell mid-surface along the z-axis, thus generalising the kinematics of flat plates to shallow shells; in this respect, the kinematic expressions presented previously remain unaffected for a shallow shell with z taken as zero along the shell mid-surface.

It is worth noting that quadratic terms of the membrane strains in (9a) take into account the effect of shell curvature, which are not necessary within a co-rotational approach but enable better accuracy with coarser meshes.

2.3 Through-thickness distribution of transverse shear strains

The face-to-core stiffness ratio (FCSR) plays an important role in the through-thickness distribution of the transverse shear stresses and strains. To illustrate this point, sandwich beams with various FCSRs have been modelled under bending with 2D plane-stress analysis, where schematic distributions of the transverse shear stress and strain with different FCSRs are depicted in Figure 3. Clearly, the distribution of the transverse shear stress changes significantly with different FCSR values. However, the transverse shear strain distribution shows that for the considered FCSR range the core sustains much larger strains than the face sheets and exhibits a near constant distribution through the constitutive layer. In addition, for a relatively small FCSR where the face sheets and the core have comparable material properties, the associated transverse shear strains then have comparable magnitude with the distribution in the face sheets exhibiting a quasi-linear pattern. Based on the observed pattern of transverse shear strains, it is assumed that in the face sheets the shear strain varies linearly from zero at the outer surface, whereas for the core the shear strain remains constant, as shown in Figure 4. The through-thickness distribution of the assumed transverse shear strain can thus be expressed as follows:

$$\boldsymbol{\varepsilon}_{s,AS}^{(k)} = \omega^{(k)} F_k(z) \boldsymbol{\varepsilon}_s^{(k)} \quad z \in \left[h_{k-}, h_{k+}\right] \tag{10}$$

where $\omega^{(k)}$ is the shear correction factor of layer (k), and $F_k(z)$ is the assumed distribution of transverse shear strains at layer (k):

$$F_1(z) = 1 + \frac{2\left(z - z^{(1)}\right)}{h_1}, \quad F_2(z) = 1, \quad F_3(z) = 1 - \frac{2\left(z - z^{(3)}\right)}{h_3} \tag{11}$$

The shear correction factors $\omega^{(k)}$ (k=1→3) can be determined from energy equivalence at the generalised stress/strain and material stress/strain levels, considering the equivalence of the generalised shear stresses and the resultant shear forces from equilibrium considerations. The employment of equivalence in transverse shear strain energy at each layer gives:

$$\boldsymbol{\varepsilon}_s^{(k)T} \mathbf{Q}_{AS}^{(k)} = \int_{h_{k-}}^{h_{k+}} \boldsymbol{\varepsilon}_{s,AS}^{(k)T} \boldsymbol{\sigma}_{s,AS}^{(k)} dz \tag{12}$$

where $\boldsymbol{\sigma}_{s,AS}^{(k)}$ are material transverse shear stresses associated with $\boldsymbol{\varepsilon}_{s,AS}^{(k)}$, and $\mathbf{Q}_{AS}^{(k)}$ are the corresponding resultant transverse shear forces, expressed as:

$$\mathbf{Q}_{AS}^{(k)} = \int_{h_{k-}}^{h_{k+}} \boldsymbol{\sigma}_{s,AS}^{(k)} dz \tag{13}$$

Substituting (11)-(12) into (13) and employing a linear constitutive relationship yield $\omega^{(1)} = \omega^{(3)} = \frac{3}{4}$ and $\omega^{(2)} = 1$.

It is important to note that the proposed approach is based on an assumed through-thickness distribution for the transverse shear strains rather than transverse shear stresses, where interlayer continuity constraints are not imposed. In addition to offering a realistic representation of the exact solution, albeit with discontinuous transvers shear stresses, this assumed strain distribution is much more practical than an assumed stress distribution when considering material nonlinearity, where the continuity requirement on transverse shear stresses necessitates an iterative solution procedure which imposes additional computational demands. Combined with the use of only two additional displacement fields associated with the proposed zigzag function, an effective sandwich shell model is obtained, which is applicable to both symmetric and asymmetric cross-sections and achieves good levels of accuracy with high computational efficiency, as demonstrated in the following section.

3 VERIFICATION OF THROUGH-THICKNESS KINEMATICS

In this section, a three-point bending problem of a sandwich beam is used to illustrate the effectiveness and efficiency of the proposed sandwich model. As depicted in Figure 5, a simply-supported sandwich beam, with length L=0.5 and depth h=0.01, is loaded with a concentrated transverse force P=–100 at midspan. The isotropic material properties of the face sheets are identical, with Young's modulus $E^{(1)} = E^{(3)} = 7\times10^{10}$ and Poisson's ratio $\nu^{(1)} = \nu^{(3)} = 0.3$. The Young's modulus and shear modulus for the core are obtained by dividing those of face sheets by the FCSR which is assumed to be respectively 1, 10, 10^2, 10^3, and 10^4. This problem is modelled with 1D 3-noded sandwich beam elements employing the proposed zigzag displacement field and transverse shear strain distribution, where shear locking is eliminated by using two-point strain mapping of the transverse shear strain. The central deflection and stress components at ¼ span are investigated:

$$\bar{u}_z = u_z\left(L/2, 0\right), \quad \bar{\sigma}_x = \sigma_x\left(L/4, h/2\right), \quad \bar{\sigma}_{xz} = \sigma_{xz}\left(L/4, 0\right)$$

where the convergent solution obtained from 2D plane-stress analysis is used as a reference. Note that this is a linear elastic problem of a perfect sandwich beam, so a linear strain-displacement relationship is considered without the inclusion of the second-order terms given in (9a).

3.1 Sandwich beam with symmetric lay-up

Here the performance of the proposed sandwich model is investigated for a symmetrically laminated sandwich beam, where the thicknesses of the three layers are assumed to be identical: $h_1 = h_2 = h_3 = h/3$. A uniform mesh of 32 sandwich beam elements which employ the proposed zigzag displacements and transverse shear strain distribution provides a convergent solution, denoted as 'present'. By restraining all additional displacement variables in the sandwich beam model, a FSDT solution is also obtained, although the assumed through-thickness distribution of the transverse shear strain proposed in this work is employed. This problem has been analysed by Hu et al. [34] in the evaluation of various lamination theories. Accordingly, the closed form solutions of other models are also provided in Table 1 for comparison. It is worth noting that the 'HSDT' model, which corresponds to

Model-2 in [34], is based on Reddy's kinematic assumptions. The 'IC-ZZT' and the 'ID-ZZT'model, corresponding to Model-5 and Model-6 in [34], are respectively a zigzag formulation with an assumed continuous transverse shear stress based on Touratier kinematic assumptions, and a layer-wise theory without imposing the conituity constraints on transverse shear stress, where the face sheets employ the Kirchhoff assumption and the core employs the Reissner-Mindlin hypothesis.

It is clear from Table 1 that the FSDT results show significant inaccuracy except for a unit FCSR value. The HSDT results also lack accuracy in the cases of very soft cores with relatively large FCSR. The proposed model, along with the IC-ZZT and ID-ZZT models are equally accurate for all the considered scenarios, which verifies the ability of the proposed zigzag function in capturing the cross-sectional warping of sandwich structures and confirms the feasibility of neglecting the continuity of transverse shear stresses in such problems.

Figure 6 compares the through-thickness distributions of the transverse shear stress at L/4 for the three models with different FCSR values. Clearly, all models provide almost the same predictions on the shear stress distribution in the core. However, the distributions in the face sheets show significant discrepancy. The IC-ZZT model provides a continuous curvilinear distribution, whereas the ID-ZZT gives zero shear stress in the face sheets due to the employment of Kirchhoff assumption in the face sheets. The proposed model yields a piecewise linear distribution of the transverse shear stress, which provides an adequate fit of the real distribution for an FCSR of 10 but indicates a big discrepancy for an FCSR of 10^4. Nevertheless, as is stated in the previous section, for sandwich structures that consist of a soft core, the core offers the dominant contribution to the transverse shear strain energy whereas the contribution from the face sheets is not of significance. On the other hand, for sandwich structures where the core is of a comparable stiffness with the face sheets, the contribution from the faces to the overall transverse shear stress becomes important. In this case, the proposed piecewise linear distribution of the transverse shear strain still provides a good approximation of the real shear stress distribution, as is illustrated in Figure 6.a. Therefore, the proposed transverse shear strain distribution is applicable to sandwich structures with a wide range of FCSRs. Furthermore, the omission of constraints on inter-laminar continuity of

the transverse shear stresses leads to a less coupled multi-layer system, which enhances computational efficiency.

3.2 Sandwich beam with asymmetric lay-up

In order to demonstrate the effectiveness of the proposed zigzag function $\Lambda(t)$ in the analysis of asymmetric cross-sections, the proposed formulation is compared against two formulations, denoted as 'MZZF1' and 'MZZF2', which add the MZZF to planar displacements which are respectively first- and second-order polynomials in z. The through-thickness variation of the transverse displacement is neglected in both models. The proposed discrete transverse shear strain distribution is employed for all formulations. Two asymmetric lay-ups are considered: (1) $h_3/h_1 = 2$ and $h_2/h_1 = 7$, and (2) $h_3/h_1 = 2$ and $h_2/h_1 = 2$.

The relative errors of the displacement and stress predictions with the considered models are shown in Table 2, from which it is clear that the proposed zigzag function provides high accuracy with various lay-ups and FCSR values. In contrast, the MZZF1 formulation, which has the same number of displacement variables as the proposed formulation, is accurate for relatively small FCSR values only. By adding a quadratic polynomial to the through-thickness distribution, the MZZF 2 formulation improves on the MZZF1 results for larger FCSR values, but still lacks accuracy for a larger FCSR, which implies the need for even higher-order z expansions and hence more zigzag displacement variables. Taking into account the number of additional zigzag displacement variables for each of the formulations (one for 'present' and 'MZZF 1', and two for 'MZZF 2'), it is evident that the proposed zigzag function $\Lambda(t)$ exhibits better efficiency than the MZZF for asymmetrically laminated sandwich structures.

4 ENHANCEMENTS FOR LARGE DISPLACEMENT ANALYSIS

In this section, enhancements are presented for the sandwich plate/shallow shell model, which upgrade a local element formulation based on this model to consider geometric nonlinearity with large displacements using the co-rotational approach. The merits of the co-rotational approach in the context of sandwich shell modelling are first discussed, which is

followed by proposing a 2D curvilinear system, so-called ‘shell’ coordinate system, which enables the effective and efficient consideration of the additional zigzag displacement fields. Nonlinear transformations between the global coordinate system and the local co-rotational system, as well as the required linear transformations between the shell coordinate system and the local co-rotational system, are finally presented.

4.1 Co-rotational approach

In formulating large displacement finite elements for small-strain problems, the relationship between the strain and displacement fields is highly nonlinear and complex if the displacement fields are referred to a fixed coordinate system, where the nonlinear strain terms arise mainly from the element rigid body rotations. In this respect, the use of a co-rotational approach [25-26] overcomes this complexity, enabling the use of a low-order strain displacement relationship at the local level, as presented for layers of shallow shells in (9), and addressing geometric nonlinearity through transformations between the local and global systems that are applied at the level of discrete element parameters.

A co-rotational system follows the current element configuration throughout the analysis, as illustrated in Section 5 for a 9-noded element, and decomposes the element motion into rigid body and strain-inducing parts, leading to an explicit relationship between the global and the local displacement parameters. The embedment of a monolithic Reissner-Mindlin formulation into the co-rotational framework is usually achieved by relating 5 local nodal displacement parameters, 3 translations and 2 rotations, to their counterparts in the global system; the exception would be where adjacent shell elements meet at an angle, in which case 3 rotational parameters would be used [28]. Since the co-rotational system follows the element configuration throughout the large displacement analysis, the transformations between the global and local element systems are nonlinear and vary from step to step.

4.2 Shell coordinate system

For the sandwich shell element formulation, if the continuity of the zigzag displacement fields is enforced via additional parameters defined in the global coordinate system, similar to

the basic nodal displacement parameters, then these would be subject to co-rotational transformations to the local system, thus imposing further computational demands. Noting that the zigzag fields describe the local effect of cross-sectional warping, it is proposed that they are defined in a 2D orthogonal curvilinear coordinate system over the shell structure, denoted as the 'shell' coordinate system, which thus follows the local co-rotational system at the element level. With the associated additional zigzag parameters defined in this shell coordinate system, continuity of the zigzag fields is ensured. Importantly, the element response associated with the zigzag parameters can thus be evaluated via a fixed linear kinematic transformation between the shell and local element systems, as elaborated in Section 4.3, rather than a varying nonlinear co-rotational transformation, which enhances the computational efficiency of the geometric nonlinear analysis of sandwich shells. Another main benefit of using a shell coordinate system relates to defining fibre orientation for composite materials, which will be discussed at the end of this sub-section.

In order to ensure continuity of the zigzag fields, a key requirement is that the 2D shell coordinate system must be associated with a unique orientation of its orthogonal directional vectors at an arbitrary point on the shell mid-surface. Besides this fundamental requirement of uniqueness, it is desirable for the 2D curvilinear shell system to be defined in a continuous manner, as illustrated by the dotted contour lines in Figure 7. For a smooth shell structure, a continuous definition of the shell system can be obtained in different ways, provided the shell surface is open. On the other hand, for a closed shell surface (e.g. a sphere), a discontinuous definition of the 2D shell coordinate system would be necessary, where the discontinuity may be localised to a single point or line. For shell structures with a folded edge, the shell system would not be uniquely defined along the fold line, though there is no requirement for continuity of the zigzag fields in such locations; a typical realistic treatment would be to restrain the additional zigzag parameters at fold lines, though a more relaxed treatment based on a free natural boundary condition for the associated zigzag forces can also be considered with the use of element-specific zigzag parameters along the folds.

With reference to the 2D curvilinear shell system (r,s) shown in Figure 7, the additional displacement zigzag parameters of an arbitrary element can be defined along the two

curvilinear directions at the node level (refer to Element I). Although the relative orientation of the shell coordinate system and local element system can vary over one element, a constant relative orientation may also be considered at the element level (refer to Element II), where all additional zigzag parameters would be assumed to accord with the surface vectors at the element centre, provided the 2D shell system is continuous. While this assumption is associated with some inaccuracy, especially for a coarse mesh, it simplifies the determination of the additional displacement fields over the element, and importantly it retains the convergence property with mesh refinement. For small-strain problems, the relative orientation of the shell coordinate system and the element local system can be assumed to remain constant throughout the analysis; hence this orientation can be established at the start of nonlinear analysis in terms of a fixed angle β for each element denoting the rotation from $\mathbf{c}_r$ to $\mathbf{c}_x$ (Figure 8).

There are many different methods for defining a unique and continuous 2D curvilinear shell system over a smooth shell structure with a continuous surface. One such definition is proposed here utilising the uniqueness and continuity property of the normal to the surface $\mathbf{c}_z^o$ of such a shell structure. In this definition, the 2D orthogonal shell system is obtained as a rotation of a user-defined reference triad $(\mathbf{c}_{\bar{X}}, \mathbf{c}_{\bar{Y}}, \mathbf{c}_{\bar{Z}})$, where the rotation that transforms $\mathbf{c}_{\bar{Z}}$ to $\mathbf{c}_z^o$ is first obtained, and this then transforms $(\mathbf{c}_{\bar{X}}, \mathbf{c}_{\bar{Y}})$ to $(\mathbf{c}_r^o, \mathbf{c}_s^o)$, respectively, as illustrated in Figure 9. The derivation of $\mathbf{c}_r^o$ is given as:

$$\mathbf{c}_r^o = \mathbf{T}_n^T \mathbf{R}_n \mathbf{T}_n \mathbf{c}_{\bar{X}} \tag{14a}$$

with

$$\mathbf{T}_n = \begin{bmatrix} \mathbf{c}_1^T \\ \mathbf{c}_2^T \\ \mathbf{c}_3^T \end{bmatrix}, \quad \mathbf{c}_1 = \mathbf{c}_z^o, \quad \mathbf{c}_3 = \frac{\mathbf{c}_{\bar{Z}} \times \mathbf{c}_z^o}{\left\| \mathbf{c}_{\bar{Z}} \times \mathbf{c}_z^o \right\|}, \quad \mathbf{c}_2 = \mathbf{c}_3 \times \mathbf{c}_1 \tag{14b}$$

and

$$\mathbf{R}_n = \begin{bmatrix} \cos(\delta) & -\sin(\delta) & 0 \\ \sin(\delta) & \cos(\delta) & 0 \\ 0 & 0 & 1 \end{bmatrix}, \quad \cos(\delta) = \mathbf{c}_{\bar{Z}} \cdot \mathbf{c}_z^o, \quad \sin(\delta) = \left\| \mathbf{c}_{\bar{Z}} \times \mathbf{c}_z^o \right\| \tag{14c}$$

where δ represents the rotation from $\mathbf{c}_{\bar{Z}}$ to $\mathbf{c}_z^o$.

For a closed shell surface, such as a spherical shell, this definition cannot be applied at the point with the normal $\mathbf{c}_z^o$ pointing just opposite to $\mathbf{c}_{\bar{Z}}$ (i.e. the two vectors are at an angle of 180°).

A second alternative definition is also proposed, as illustrated in Figure 10, where $\mathbf{c}_s^o$ in the initial undeformed configuration is considered to be a projection of a user-defined vector **n** on the shell surface and $\mathbf{c}_r^o$ is obtained from:

$$\mathbf{c}_r^o = \frac{\mathbf{n} \times \mathbf{c}_z^o}{\left\| \mathbf{n} \times \mathbf{c}_z^o \right\|} \tag{15}$$

This definition can be used to generate a continuous 2D shell system provided a vector **n** can be specified which is not orthogonal to the shell surface at any point. For some curved shells with open surfaces, such as a hemi-spherical shell, this is not possible, hence a discontinuous definition of the 2D shell system will be required at the point(s) where the shell surface is normal to **n**.

Figure 11 illustrates a third alternative definition, which is similar to the previous one except that the projection vector **n** points from the shell surface to a reference point O, with similar restrictions to the second alternative in relation to the case where **n** may be orthogonal to the shell surface.

It is worth noting that in cases where a discontinuous definition of the 2D shell coordinate system is inevitable, a unique orientation of $(\mathbf{c}_r^o, \mathbf{c}_s^o)$ can still be prescribed at the point(s) of singularity, and the additional displacement zigzag parameters of the surrounding elements can then be defined at the node level (refer to Element I in Figure 7).

Besides the enhancement of the computational efficiency in large displacement analysis, the utilisation of the 2D curvilinear shell system provides the additional benefit of providing the orientation of material fibres in relation to the local element coordinate system when composite materials are considered. In a general arbitrary mesh, the direction of the element local system can be arbitrarily distributed throughout the mesh, depending on the employed definition of the co-rotational approach, the element configuration and nodal ordering.

However, with the use of a continuous 2D shell system, the material fibre orientation can be defined with respect to the shell r-axis, as described by the continuous vector $\mathbf{c}_r^o$ in the initial undeformed configuration. By denoting $\alpha^{(k)}$ to be the angle from the shell directional vector $\mathbf{c}_r^o$ to the material fibre direction at layer (k), $\mathbf{c}_r^{o*(k)}$, the angle from the local element x-axis to the material fibre direction is simply obtained as (Figure 12):

$$\varphi^{(k)} = \alpha^{(k)} - \beta \tag{16}$$

This then allows the constitutive material response to be established in the local element system through appropriate strain/stress transformations.

4.3 Kinematic transformations between global, local and shell systems

As already noted, the present work proposes the use of a co-rotational framework for upgrading the low-order sandwich plate/shallow shell model to geometrically nonlinear analysis, where the nonlinear kinematic transformations between the global and local element systems are conveniently restricted to the basic nodal displacement and rotational parameters. On the other hand, the additional zigzag displacement parameters, which describe the local cross-sectional warping behaviour only, are defined in a specific shell system which follow the local element system at a constant orientation, and are therefore excluded from the co-rotational transformations.

The kinematic relationship between local displacement variables and their global counterparts depends on the employed definition of the co-rotational approach and the sequence of nodal numbering. This is illustrated for a 9-noded shell element using the bisector co-rotational system definition [25,28] in Section 5.1. On the other hand, the relationship between the zigzag displacements defined in the shell and local systems is linear for small-strain problems, where the following is employed to transform the additional fields from the shell system to the local element system:

$$\begin{Bmatrix} \vartheta_x \\ \vartheta_y \end{Bmatrix} = \begin{bmatrix} \hat{c} & \hat{s} \\ -\hat{s} & \hat{c} \end{bmatrix} \begin{Bmatrix} \vartheta_r \\ \vartheta_s \end{Bmatrix}, \quad \hat{c} = \cos(\beta), \quad \hat{s} = \sin(\beta) \tag{17}$$

in which $\langle \vartheta_r , \vartheta_s \rangle$ are additional zigzag displacement fields defined in the curvilinear shell system, and angle β is the relative orientation of the two systems obtained at the start of analysis.

Note that (17) is most effectively accounted for in the kinematic description of (7) and (8) by re-defining the additional zigzag fields $\mathbf{u}_a$ in the shell coordinate system, i.e. $\mathbf{u}_a = \langle \vartheta_r , \vartheta_s \rangle^T$, and adjusting the transformation matrix $\mathbf{T}_a^{(k)}$ to:

$$\mathbf{T}_a^{(k)} = \begin{bmatrix} \hat{c}\Lambda^{(k)} & \hat{s}\Lambda^{(k)} \\ -\hat{s}\Lambda^{(k)} & \hat{c}\Lambda^{(k)} \\ 0 & 0 \\ \hat{c}\lambda^{(k)} & \hat{s}\lambda^{(k)} \\ -\hat{s}\lambda^{(k)} & \hat{c}\lambda^{(k)} \end{bmatrix} \tag{18}$$

This works well provided the shell system is continuous over the element, in which case the response is convergent with mesh refinement even where any variation in the relative orientation of the shell and local element system is ignored for curved shells, with $(\hat{c}, \hat{s})$ assumed constant over the element. On the other hand, when the local shell system is discontinuous, as would be the case at specific locations for a closed shell structure, the most effective approach would be to transform the nodal zigzag displacement parameters from the node-specific shell system to the local element system, with the local parameters then used to define the local zigzag fields $\langle \vartheta_x , \vartheta_y \rangle$ directly. The latter approach is utilised for generality in the following application to a 9-noded sandwich shell element.

5 APPLICATION TO 9-NODED SHELL ELEMENT

In this section, the application of the proposed sandwich model is illustrated for a 9-noded co-rotational shell element [27-28], noting that it can also be similarly applied to other shell elements of different order and shape. A bisector co-rotational framework, shown in Figure 13, is employed for large displacement analysis, where basic local displacements $\mathbf{u}_c$ are related to the global parameters according to nonlinear kinematic transformations that exclude the influence of rigid body rotations at the local element level. Additional zigzag displacements $\mathbf{u}_a$ are defined in the 2D curvilinear shell system, and their associated resistance forces are readily assembled without the need for co-rotational transformation. At

each layer (k), the Mixed Interpolation of Tensorial Components (MITC) method [32-33] is employed for alleviating locking. The development of the 9-noded element within the bisector co-rotational framework for application to sandwich shells according to the proposed approach is elaborated in the following sub-sections.

5.1 Bisector co-rotational system

Figure 13 illustrates the co-rotational framework used for the 9-noded shell element, where (X, Y, Z) and (x, y, z) refer to the global and local co-rotational coordinate systems, respectively. The x- and y-axes of the local co-rotational system are defined such that they coincide with the bisectors of the diagonal vectors generated from the four corner nodes in the current unknown configuration [25]. Three translational and two rotational global parameters are defined in the global coordinate system, which are then transformed to five basic parameters $(u_{x0}, u_{y0}, u_{z0}, \theta_x, \theta_y)$ in the co-rotational system. The triad of this co-rotational system and the relevant global-local displacement transformations are provided in Appendix B. By filtering out the rigid body rotations, the co-rotational approach shifts the large-displacement/small-strain problem to a small-displacement/small-strain problem at the local element level, thus allowing the employment of low-order kinematics, such as proposed in Section 3 for sandwich shells.

5.2 Local element kinematics

Local and additional parameters are respectively defined as $\mathbf{U}_C = \left\langle \mathbf{U}_{C1}^T, \cdots, \mathbf{U}_{Ci}^T, \cdots, \mathbf{U}_{C9}^T \right\rangle^T$ and $\mathbf{U}_A = \left\langle \mathbf{U}_{A1}^T, \cdots, \mathbf{U}_{Ai}^T, \cdots, \mathbf{U}_{A9}^T \right\rangle^T$, where $\mathbf{U}_{Ci}$ and $\mathbf{U}_{Ai}$ contain respectively five co-rotational nodal parameters and two additional parameters, which are expressed as $\mathbf{U}_{Ci} = \left\langle u_{x0,i}, u_{y0,i}, u_{z0,i}, \theta_{x,i}, \theta_{y,i} \right\rangle^T$ and $\mathbf{U}_{Ai} = \left\langle \vartheta_{r,i}, \vartheta_{s,i} \right\rangle^T$. The pseudo nodal parameters at layer (k), which are defined as $\mathbf{U}^{(k)} = \left\langle \mathbf{U}_1^{(k)}, \cdots, \mathbf{U}_i^{(k)}, \cdots, \mathbf{U}_9^{(k)} \right\rangle^T$ with $\mathbf{U}_i^{(k)} = \left\langle u_{x,i}^{(k)}, u_{y,i}^{(k)}, u_{z,i}^{(k)}, \theta_{x,i}^{(k)}, \theta_{y,i}^{(k)} \right\rangle^T$, can be obtained from the following relationship:

$$\mathbf{U}^{(k)} = \mathbf{T}_C^{(k)} \mathbf{U}_C + \mathbf{T}_A^{(k)} \mathbf{U}_A \tag{19}$$

$$\mathbf{T}_C^{(k)} = \begin{bmatrix} \mathbf{T}_c^{(k)} & & \mathbf{0} \\ & \ddots & \\ \mathbf{0} & & \mathbf{T}_c^{(k)} \end{bmatrix}_{(45\times45)}, \quad \mathbf{T}_A^{(k)} = \begin{bmatrix} \mathbf{T}_a^{(k)} & & \mathbf{0} \\ & \ddots & \\ \mathbf{0} & & \mathbf{T}_a^{(k)} \end{bmatrix}_{(45\times18)} \tag{20}$$

where $\mathbf{T}_c^{(k)}$ and $\mathbf{T}_a^{(k)}$ are given in (8a) and (18), respectively. Note that $\mathbf{T}_A^{(k)}$ applies to a continuous shell system definition, ignoring the change of $(\hat{c},\hat{s})$ over the element, but it can be easily modified to account for different shell orientation vectors at individual nodes by adjust the component diagonal $\mathbf{T}_a^{(k)}$ sub-matrices accordingly.

Isoparametric mapping of element geometry and pseudo displacement fields is performed with the use of quadratic Lagrangian shape functions in the natural coordinate system (ξ,η,ζ):

$$\phi_i(\xi,\eta)=\frac{(\xi-\xi_i')(\xi-\xi_i'')}{(\xi_i-\xi_i')(\xi_i-\xi_i'')}\cdot\frac{(\eta-\eta_i')(\eta-\eta_i'')}{(\eta_i-\eta_i')(\eta_i-\eta_i'')}\quad (i=1\rightarrow 9) \tag{21}$$

in which $(\xi_i\neq\xi_i'\neq\xi_i'')=-1,0,1$; $(\eta_i\neq\eta_i'\neq\eta_i'')=-1,0,1$; (ξ_i,η_i) represent the natural coordinates of node i. With the mapped pseudo displacement fields, the generalised strains of each layer (k) are calculated via (9).

5.3 Material constitutive response

For isotropic and orthotropic materials, the material stresses are obtained from the following equations:

$$\boldsymbol{\sigma}_p^{(k)}=\mathbf{C}_p^{(k)}\boldsymbol{\varepsilon}_p^{(k)},\quad \boldsymbol{\sigma}_{s,AS}^{(k)}=\mathbf{C}_s^{(k)}\boldsymbol{\varepsilon}_{s,AS}^{(k)} \tag{22}$$

where $\boldsymbol{\varepsilon}_p^{(k)}$ are planar material strains of layer (k), given as:

$$\boldsymbol{\varepsilon}_p^{(k)}=\boldsymbol{\varepsilon}_m^{(k)}+\frac{h_k}{2}\zeta^{(k)}\boldsymbol{\varepsilon}_b^{(k)},\quad \zeta^{(k)}=\frac{2(z-z^{(k)})}{h_k}\quad z\in\left[h_{k-},h_{k+}\right] \tag{23}$$

$\boldsymbol{\varepsilon}_{s,AS}^{(k)}$ represents the assumed transverse shear strains as presented in Section 3.3; $\mathbf{C}_p^{(k)}$ and $\mathbf{C}_s^{(k)}$ are material constitutive matrices for planar and transverse shear stresses/strains of layer (k).

For isotropic materials, $\mathbf{C}_p^{(k)}$ and $\mathbf{C}_s^{(k)}$ are given as:

$$\mathbf{C}_p^{(k)}=\frac{E^{(k)}}{1-\nu^{(k)2}}\begin{bmatrix}1 & \nu^{(k)} & 0\\ \nu^{(k)} & 1 & 0\\ 0 & 0 & \dfrac{1-\nu^{(k)}}{2}\end{bmatrix},\quad \mathbf{C}_s^{(k)}=\frac{E^{(k)}}{2(1+\nu^{(k)})}\begin{bmatrix}1 & 0\\ 0 & 1\end{bmatrix} \tag{24}$$

with $E^{(k)}$ and $\nu^{(k)}$ representing the Young's modulus and Poisson's ratio of layer (k).

For orthotropic materials, $\mathbf{C}_p^{(k)}$ and $\mathbf{C}_s^{(k)}$ are obtained from:

$$\mathbf{C}_p^{(k)} = \mathbf{T}_p^{*(k)T}\,\mathbf{C}_p^{*(k)}\,\mathbf{T}_p^{*(k)}, \quad \mathbf{C}_s^{(k)} = \mathbf{T}_s^{*(k)T}\,\mathbf{C}_s^{*(k)}\,\mathbf{T}_s^{*(k)} \tag{25}$$

$$\mathbf{C}_p^{*(k)} = \begin{bmatrix} \dfrac{E_1^{(k)}}{1-\nu_{12}^{(k)}\nu_{21}^{(k)}} & \dfrac{\nu_{12}^{(k)}E_2^{(k)}}{1-\nu_{12}^{(k)}\nu_{21}^{(k)}} & 0 \\ \dfrac{\nu_{12}^{(k)}E_2^{(k)}}{1-\nu_{12}^{(k)}\nu_{21}^{(k)}} & \dfrac{E_2^{(k)}}{1-\nu_{12}^{(k)}\nu_{21}^{(k)}} & 0 \\ 0 & 0 & G_{12}^{(k)} \end{bmatrix}, \quad \mathbf{C}_s^{*(k)} = \begin{bmatrix} G_{13}^{(k)} & 0 \\ 0 & G_{23}^{(k)} \end{bmatrix} \tag{26}$$

$$\mathbf{T}_p^{*(k)} = \begin{bmatrix} \cos^2(\varphi^{(k)}) & \sin^2(\varphi^{(k)}) & \dfrac{1}{2}\sin(2\varphi^{(k)}) \\ \sin^2(\varphi^{(k)}) & \cos^2(\varphi^{(k)}) & -\dfrac{1}{2}\sin(2\varphi^{(k)}) \\ -\sin(2\varphi^{(k)}) & \sin(2\varphi^{(k)}) & \cos(2\varphi^{(k)}) \end{bmatrix}, \quad \mathbf{T}_s^{*(k)} = \begin{bmatrix} \cos(\varphi^{(k)}) & \sin(\varphi^{(k)}) \\ -\sin(\varphi^{(k)}) & \cos(\varphi^{(k)}) \end{bmatrix} \tag{27}$$

where $\mathbf{C}_p^{*(k)}$ and $\mathbf{C}_s^{*(k)}$ are the material constitutive matrices in the material coordinate system; $\mathbf{T}_p^{*(k)}$ and $\mathbf{T}_s^{*(k)}$ are constitutive transformation matrices from the material coordinate system to the local element system; $\varphi^{(k)}$ is the angle from the element coordinate system to the material coordinate system at layer (k), as given in (16).

Although only isotropic and orthotropic material models are considered in this paper, other material models may also be used.

5.4 Local resistance forces and stiffness

Local resistance forces of the sandwich shell element are obtained from the internal virtual work of the element, which is expressed as:

$$\delta\mathbf{U}_C^T\,\mathbf{f}_C + \delta\mathbf{U}_A^T\,\mathbf{f}_A = \sum_{k=1}^{3}\int_{\Omega^e}\left(\int_{h_{k-}}^{h_{k+}}\left(\delta\boldsymbol{\varepsilon}_p^{(k)T}\boldsymbol{\sigma}_p^{(k)} + \delta\boldsymbol{\varepsilon}_{s,AS}^{(k)T}\boldsymbol{\sigma}_{s,AS}^{(k)}\right)dz\right)d\Omega^e \quad \forall\left(\delta\mathbf{U}_C, \delta\mathbf{U}_A\right) \tag{28}$$

where integration is performed over the local element domain Ω^e; $\mathbf{f}_C$ and $\mathbf{f}_A$ are resistance forces with respect to basic parameters $\mathbf{U}_C$ and additional parameters $\mathbf{U}_A$, respectively.

By defining the generalised membrane, bending, and transverse shear stresses as follows:

$$\mathbf{F}^{(k)} = \int_{h_{k-}}^{h_{k+}}\boldsymbol{\sigma}_p^{(k)}dz = h_k\mathbf{C}_p^{(k)}\boldsymbol{\varepsilon}_m^{(k)} \tag{29}$$

$$\mathbf{M}^{(k)} = \int_{h_{k-}}^{h_{k+}} \boldsymbol{\sigma}_p^{(k)} \left(z - z^{(k)} \right) dz = \frac{1}{12} h_k^3 \mathbf{C}_p^{(k)} \boldsymbol{\varepsilon}_b^{(k)} \tag{30}$$

and elaborating the generalised transverse shear stresses in (16) as:

$$\mathbf{Q}_{AS}^{(k)} = \int_{h_{k-}}^{h_{k+}} \mathbf{C}_s^{(k)} \boldsymbol{\varepsilon}_{s,AS}^{(k)} dz = \omega^{(k)} h_k \mathbf{C}_s^{(k)} \boldsymbol{\varepsilon}_s^{(k)} \tag{31}$$

Equation (28) is expressed in the following form:

$$\delta \mathbf{U}_C^T \mathbf{f}_C + \delta \mathbf{U}_A^T \mathbf{f}_A = \sum_{k=1}^{3} \int_{\Omega^e} \left(\delta \boldsymbol{\varepsilon}_m^{(k)T} \mathbf{F}^{(k)} + \delta \boldsymbol{\varepsilon}_b^{(k)T} \mathbf{M}^{(k)} + \delta \boldsymbol{\varepsilon}_s^{(k)T} \mathbf{Q}_{AS}^{(k)} \right) d\Omega^e \quad \forall \left(\delta \mathbf{U}_C, \delta \mathbf{U}_A \right) \tag{32}$$

Equation (32) can be further manipulated to:

$$\begin{aligned} &\delta \mathbf{U}_C^T \mathbf{f}_C + \delta \mathbf{U}_A^T \mathbf{f}_A = \\ &\sum_{k=1}^{3} \left(\delta \mathbf{U}_C^T \mathbf{T}_C^{(k)T} + \delta \mathbf{U}_A^T \mathbf{T}_A^{(k)T} \right) \int_{\Omega^e} \left(\mathbf{B}_m^{(k)T} \mathbf{D}_m^{(k)} \boldsymbol{\varepsilon}_m^{(k)} + \mathbf{B}_b^{(k)T} \mathbf{D}_b^{(k)} \boldsymbol{\varepsilon}_b^{(k)} + \mathbf{B}_s^{(k)T} \mathbf{D}_s^{(k)} \boldsymbol{\varepsilon}_s^{(k)} \right) d\Omega^e \\ &\qquad \forall \left(\delta \mathbf{U}_C, \delta \mathbf{U}_A \right) \end{aligned} \tag{33}$$

where $\mathbf{B}_m^{(k)}$, $\mathbf{B}_b^{(k)}$ and $\mathbf{B}_s^{(k)}$ are the first derivatives of the generalised strains at layer (k) with respect to pseudo parameters $\mathbf{U}^{(k)}$; $\mathbf{D}_m^{(k)}$, $\mathbf{D}_b^{(k)}$, and $\mathbf{D}_s^{(k)}$ are generalised constitutive matrices at layer (k), which are expressed as:

$$\mathbf{D}_m^{(k)} = h_k \mathbf{C}_p^{(k)}, \quad \mathbf{D}_b^{(k)} = \frac{1}{12} h_k^3 \mathbf{C}_p^{(k)}, \quad \mathbf{D}_s^{(k)} = \omega^{(k)} h_k \mathbf{C}_s^{(k)} \tag{34}$$

In order to address the locking phenomenon in the 9-noded shell element, the MITC9 [32-33] strain-mapping approach is employed in the local formulation of each constitutive layer. Figure 14 shows the positions of the tying points for different strain components, and the associated interpolation functions for the covariant strains can be found elsewhere [32]. In order to allow the MITC9 element to pass the patch tests, a constant Jacobian matrix is required in the strain-mapping steps [33]. The MITC9 application to a monolithic co-rotational shell element is provided in [28], which is employed here at each individual layer for the sandwich shell element. After the application of the tying and mapping scheme at each constitutive layer, the conforming strains $\boldsymbol{\varepsilon}_m^{(k)}$, $\boldsymbol{\varepsilon}_b^{(k)}$ and $\boldsymbol{\varepsilon}_s^{(k)}$, and the matrices $\mathbf{B}_m^{(k)}$, $\mathbf{B}_b^{(k)}$ and $\mathbf{B}_s^{(k)}$ in (33) are replaced with $\tilde{\boldsymbol{\varepsilon}}_m^{(k)}$, $\tilde{\boldsymbol{\varepsilon}}_b^{(k)}$, $\tilde{\boldsymbol{\varepsilon}}_s^{(k)}$, $\tilde{\mathbf{B}}_m^{(k)}$, $\tilde{\mathbf{B}}_b^{(k)}$ and $\tilde{\mathbf{B}}_s^{(k)}$, where '$\tilde{\ }$' denotes the application of the MITC9 strain-mapping procedure at each individual layer.

Considering (33), the total resistance forces of the shell element associated with the local nodal parameters $\mathbf{U}_C$ and the additional parameters $\mathbf{U}_A$ are thus obtained as:

$$\mathbf{f}_C = \sum_{k=1}^{3}\left(\mathbf{T}_C^{(k)T}\mathbf{f}^{(k)}\right), \quad \mathbf{f}_A = \sum_{k=1}^{3}\left(\mathbf{T}_A^{(k)T}\mathbf{f}^{(k)}\right) \tag{35}$$

where $\mathbf{f}^{(k)}$ is the vector of pseudo nodal forces at layer (k), expressed as:

$$\mathbf{f}^{(k)} = \int_{\Omega^e}\left(\tilde{\mathbf{B}}_m^{(k)T}\mathbf{D}_m^{(k)}\tilde{\boldsymbol{\varepsilon}}_m^{(k)} + \tilde{\mathbf{B}}_b^{(k)T}\mathbf{D}_b^{(k)}\tilde{\boldsymbol{\varepsilon}}_b^{(k)} + \tilde{\mathbf{B}}_s^{(k)T}\mathbf{D}_s^{(k)}\tilde{\boldsymbol{\varepsilon}}_s^{(k)}\right)d\Omega^e \tag{36}$$

Furthermore, the local tangent stiffness matrices of the element are obtained as:

$$\mathbf{k}_C = \frac{\partial \mathbf{f}_C}{\partial \mathbf{U}_C^T} = \sum_{k=1}^{3}\left(\mathbf{T}_C^{(k)T}\mathbf{k}^{(k)}\mathbf{T}_C^{(k)}\right), \quad \mathbf{k}_A = \frac{\partial \mathbf{f}_A}{\partial \mathbf{U}_A^T} = \sum_{k=1}^{3}\left(\mathbf{T}_A^{(k)T}\mathbf{k}^{(k)}\mathbf{T}_A^{(k)}\right) \tag{37a}$$

$$\mathbf{k}_{CA} = \mathbf{k}_{AC}^T = \frac{\partial \mathbf{f}_C}{\partial \mathbf{U}_A^T} = \sum_{k=1}^{3}\left(\mathbf{T}_C^{(k)T}\mathbf{k}^{(k)}\mathbf{T}_A^{(k)}\right) \tag{37b}$$

where $\mathbf{k}^{(k)}$ is the pseudo local stiffness of layer (k), which is expressed as:

$$\mathbf{k}^{(k)} = \int_{\Omega^e}\left(\tilde{\mathbf{B}}_m^{(k)T}\mathbf{D}_m^{(k)}\tilde{\mathbf{B}}_m^{(k)} + \tilde{\mathbf{B}}_b^{(k)T}\mathbf{D}_b^{(k)}\tilde{\mathbf{B}}_b^{(k)} + \tilde{\mathbf{B}}_s^{(k)T}\mathbf{D}_s^{(k)}\tilde{\mathbf{B}}_s^{(k)} + \frac{\partial^2\tilde{\boldsymbol{\varepsilon}}_m^{(k)T}}{\partial\mathbf{U}^{(k)}\partial\mathbf{U}^{(k)T}}\mathbf{D}_m^{(k)}\tilde{\boldsymbol{\varepsilon}}_m^{(k)}\right)d\Omega^e \tag{38}$$

5.5 Co-rotational transformation of resistance forces and stiffness

In accordance with the co-rotational approach, the local resistance forces and stiffness matrices of the sandwich shell element are transformed to the corresponding global system entities before assembly at the overall structural level. It is important to note that the relationship between additional parameters defined in the shell system and their counterparts in the element local system is directly considered by incorporating $(\hat{c},\hat{s})$ into $\mathbf{T}_a^{(k)}$, as given in (18). Furthermore, the resistant force vector $\mathbf{f}_A$ and the stiffness matrix $\mathbf{k}_A$ are excluded from the co-rotational transformations, since the associated zigzag parameters are defined in the shell system at the overall structural level.

The transformation of the resistant forces and stiffness matrices to the global coordinate system are given as:

$$\mathbf{f}_G = \mathbf{T}^T\mathbf{f}_C \tag{39}$$

$$\mathbf{k}_{\mathrm{G}} = \frac{\partial \mathbf{f}_{\mathrm{G}}}{\partial \mathbf{U}_{\mathrm{G}}^{\mathrm{T}}} = \mathbf{T}^{\mathrm{T}} \mathbf{k}_{\mathrm{C}} \mathbf{T} + \frac{\partial^2 \mathbf{U}_{\mathrm{C}}^{\mathrm{T}}}{\partial \mathbf{U}_{\mathrm{G}} \partial \mathbf{U}_{\mathrm{G}}^{\mathrm{T}}} \mathbf{f}_{\mathrm{C}} \tag{40a}$$

$$\mathbf{k}_{\mathrm{GA}} = \mathbf{k}_{\mathrm{AG}}^{\mathrm{T}} = \frac{\partial \mathbf{f}_{\mathrm{G}}}{\partial \mathbf{U}_{\mathrm{A}}^{\mathrm{T}}} = \mathbf{T}^{\mathrm{T}} \mathbf{k}_{\mathrm{CA}} \tag{40b}$$

in which $\mathbf{T}$ is the nodal displacement transformation matrix from global parameters $\mathbf{U}_{\mathrm{G}}$ to co-rotational parameters $\mathbf{U}_{\mathrm{C}}$ [25, 28], defined as:

$$\mathbf{T} = \frac{\partial \mathbf{U}_{\mathrm{C}}}{\partial \mathbf{U}_{\mathrm{G}}^{\mathrm{T}}} \tag{41}$$

6 NUMERICAL EXAMPLES

The proposed sandwich shell modelling approach, instantiated for a 9-noded element and referred to as 'SS-MITC9', has been implemented in ADAPTIC [35] v2.14.2, which is used hereafter in several verification examples to demonstrate the accuracy of the newly developed approach for both symmetrically and asymmetrically laminated sandwich plates and shells.

6.1 Sandwich plate under bidirectional sinusoidal loading

A square sandwich plate, simply-supported along all four edges, is subjected to a bidirectional sinusoidal transverse loading $p = p_0 \sin(\pi x/a)\sin(\pi y/a)$, as depicted in Figure 15, where consideration is given here to the linear elastic response. The edge length of the square plate is a, and the thickness is h (with $h_1 = h_3 = 0.1h$ and $h_2 = 0.8h$). The material parameters of the layers are given as:

Core: $E_1^{(2)} = E_2^{(2)} = 0.4\times10^5, G_{12}^{(2)} = 0.16\times10^5, G_{13}^{(2)} = G_{23}^{(2)} = 0.6\times10^5, \nu_{12}^{(2)} = 0.25.$

Face: $E_1^{(1,3)} = 2.5\times10^7, E_2^{(1,3)} = 1.0\times10^6, G_{12}^{(1,3)} = G_{13}^{(1,3)} = 0.5\times10^6, G_{23}^{(1,3)} = 0.2\times10^6, \nu_{12}^{(1,3)} = 0.25.$

where the 1- and 2- material directions for the layers are aligned respectively with the x- and y-axes.

Different length-to-thickness ratios are considered, where due to symmetry only a quarter of the plate is analysed with a uniform 8×8 mesh of the SS-MITC9 element (289 nodes, and 7 DOFs/node), which provides a convergent solution. In this model, the shell system can be obtained according to the approach illustrated in Figure 9 with the reference triad $(\mathbf{c}_{\bar{\mathrm{X}}}, \mathbf{c}_{\bar{\mathrm{Y}}}, \mathbf{c}_{\bar{\mathrm{Z}}})$ aligned with the global system triad, in which case the curvilinear shell triad maintains the same (x,y) directions for all elements. The elasticity solution by Pagano [36] is

used as a reference solution. Results from other researchers are also considered, including the FSDT solution by Pandya and Kant [2] using a 5×5 mesh of 9-noded elements (121 nodes, and 3 DOFs/node), the solution by Balah and Al-Ghamedy [37] using a 16×16 mesh of 4-noded elements based on a third-order shear deformation theory (TSDT, 289 nodes, and 7 DOFs/node), the LWT solution by Thai et al. [38] employing an isogeometric approach with 17×17 quartic B-spline basis for the whole plate (7 DOFs/node), and a higher-order ZZT solution by Pandit et al. [8] with a 12×12 mesh of 9-noded elements for the whole plate (625 nodes, and 11 DOFs/node). The full results are provided in Table 3. Key displacement and stress values are assessed with the corresponding dimensionless results defined as follows:

$$\bar{u}_z = \frac{100E_2^{(1,3)}h^3 u_z\left(\frac{a}{2},\frac{a}{2},0\right)}{p_0 a^4},\ \bar{\sigma}_x = \frac{h^2\sigma_x\left(\frac{a}{2},\frac{a}{2},\frac{h}{2}\right)}{p_0 a^2},\ \bar{\sigma}_y = \frac{h^2\sigma_y\left(\frac{a}{2},\frac{a}{2},\frac{h}{2}\right)}{p_0 a^2}$$

$$\bar{\sigma}_{xz} = \frac{h\sigma_{xz}\left(0,\frac{a}{2},0\right)}{p_0 a},\ \bar{\sigma}_{yz} = \frac{h\sigma_{yz}\left(\frac{a}{2},0,0\right)}{p_0 a},\ \bar{\sigma}_{xy} = \frac{h^2\sigma_{xy}\left(0,0,\frac{h}{2}\right)}{p_0 a^2}$$

It is concluded from Table 3 that all the theories agree well for the thin sandwich plate (a/h=100), in particular the deflection and planar stresses. As (a/h) decreases, the zigzag effect on the plate behaviour becomes significant, which leads to a noticeable deviation of the FSDT solution from the reference solution for moderately thick sandwich plates (a/h=10). Although the TSDT solution provides improved accuracy over the FSDT results, its predictions are still not as accurate as those of the other three models owing to the employment of assumed displacement modes at the multi-layer level rather than at the layer level. The SS-MITC9 model, which describes the zigzag effect with only two additional displacement fields, exhibits comparable capability with the LWT, and ZZT models, both of which assume four additional displacement fields, in the approximation of both the deflection and stress components of moderately thick plates, which indicates the validity of the assumed additional displacement modes and distribution of transverse shear strains. Figure 16 depicts the through-thickness distributions of the considered stress components for the cases a/h=10 and 20, where the results of the SS-MITC9 model agree well with the LWT results by Thai et al. [38], with more realistic distributions of transverse shear strains.

6.2 Sandwich plate under uniformly distributed transverse loading

A simply-supported square sandwich plate is subjected to a uniformly distributed transverse loading p_0, as shown in Figure 17, where consideration is again given to the linear elastic response. The length-to-thickness ratio (a/h) of the plate is fixed to 10, and the thickness of each face sheet is 0.1h. The elastic constitutive matrix of the core is:

$$\mathbf{C}^{(2)} = \begin{bmatrix} \mathbf{C}_p^{(2)} & \mathbf{0} \\ \mathbf{0} & \mathbf{C}_s^{(2)} \end{bmatrix} = \left[\begin{array}{ccc|cc} 0.999781 & 0.231192 & 0 & 0 & 0 \\ 0.231192 & 0.524866 & 0 & 0 & 0 \\ 0 & 0 & 0.262931 & 0 & 0 \\ \hline 0 & 0 & 0 & 0.266810 & 0 \\ 0 & 0 & 0 & 0 & 0.159914 \end{array}\right]$$

The constitutive matrix of the faces is given by $\mathbf{C}^{(1)} = \mathbf{C}^{(3)} = \mathrm{FCSR} \cdot \mathbf{C}^{(2)}$, where the value of FCSR is alternatively taken as 5, 10, and 15. A quarter of the plate is modelled due to symmetry, and an 8×8 mesh of the SS-MITC9 elements (289 nodes, and 7 DOFs/node) provides a convergent solution. In this model, the shell system is aligned with the (x,y) planar coordinate system. The dimensionless transverse displacement and stresses at some key positions are assessed, which are defined as follows:

$$\bar{u}_z = \frac{0.999781 u_z\left(\frac{a}{2},\frac{a}{2},0\right)}{p_0 h},\ \bar{\sigma}_x^1 = \frac{\sigma_x^{(3)}\left(\frac{a}{2},\frac{a}{2},\frac{h}{2}\right)}{p_0},\ \bar{\sigma}_x^2 = \frac{\sigma_x^{(3)}\left(\frac{a}{2},\frac{a}{2},\frac{4h}{10}\right)}{p_0}$$

$$\bar{\sigma}_x^3 = \frac{\sigma_x^{(2)}\left(\frac{a}{2},\frac{a}{2},\frac{4h}{10}\right)}{p_0},\ \bar{\sigma}_y^1 = \frac{\sigma_y^{(3)}\left(\frac{a}{2},\frac{a}{2},\frac{h}{2}\right)}{p_0},\ \bar{\sigma}_y^2 = \frac{\sigma_y^{(3)}\left(\frac{a}{2},\frac{a}{2},\frac{4h}{10}\right)}{p_0}$$

$$\bar{\sigma}_y^3 = \frac{\sigma_y^{(2)}\left(\frac{a}{2},\frac{a}{2},\frac{4h}{10}\right)}{p_0},\ \bar{\sigma}_{xz} = \frac{\sigma_{xz}\left(0,\frac{a}{2},0\right)}{p_0}$$

The results of the SS-MITC9 model are shown in Table 4, which are compared against the exact solution by Srinivas and Rao [39]. The FSDT solution (121 nodes, and 3 DOFs/node) and HSDT solution (121 nodes, and 5 DOFs/node) by Pandya and Kant [2] and the LWT solution by Ferreira et al. [40] using a pseudo-spectral method (7 DOFs/node) are also given for comparison purposes.

It is clear that as FCSR increases, the difference in the material properties between the faces and the core induces a significant zigzag effect of the sandwich plate, which leads to a deteriorating performance of the FSDT solution. The HSDT solution, despite showing an improvement in accuracy over the FSDT solution, still does not capture well the response of the sandwich shell, particularly when the stiffness ratio FCSR is relatively large. The 8×8 mesh of the SS-MITC9 elements provides better accuracy than the LWT solution in the approximation of both displacement and stresses owing to the employment of the assumed transverse shear strain distribution.

6.3 Asymmetrically laminated sandwich plate under loading

Consideration is given here to an asymmetrically laminated three-layered sandwich plate with sheet thicknesses of $h_1 = h/10$, $h_2 = 7h/10$, and $h_3 = 2h/10$. The plate, which has an aspect ratio of b/a = 3, is simply supported on all four edges and transversely loaded with a bidirectional sinusoidal pressure $p = p_0 \sin(\pi x/a)\sin(\pi y/b)$ on the top surface, as shown in Figure 18. All layers are made of isotropic materials, where the modular ratio between the face sheets is $E^{(1)}/E^{(3)} = 5/4$, and the Poisson's ratios of all layers are 0.34. Four scenarios are considered to evaluate the performance of the proposed sandwich shell model in the simulation of thick/thin plate problems with insignificant/significant through-thickness material change: a/h=4, 100, and $FCSR = E^{(1)}/E^{(2)} = 10, 10^5$.

The elasticity solution for this linear elastic problem has been given by Demasi [41]. Brischetto et al. [15] also analysed this problem with EDZ models, where the number of displacement fields for the considered models are listed in Table 5. An 8×8 mesh of the SS-MITC9 elements provides a convergent solution, where the curvilinear shell system is aligned with the (x, y) planar coordinate system. The results are compared against the closed form solutions of the EDZ models [15] in terms of dimensionless displacement and stress values, which are defined as:

$$\bar{u}_z = \frac{100 u_z E^{(2)}}{p_0 h (a/h)^4}, \quad \bar{\sigma}_x = \frac{\sigma_x}{p_0 (a/h)^2}, \quad \bar{\sigma}_{xz} = \frac{\sigma_{xz}}{p_0 (a/h)}$$

The values of the non-dimensional central deflection $\bar{u}_z(a/2, b/2)$ at the bottom of the upper sheet obtained with the considered models are listed in Table 6 along with the reference elasticity solution by Demasi [41]. Clearly, the SS-MITC9 model provides a much closer estimation of deflection than the EDZ1 model and even better results than the EDZ4 predictions, which utilise more displacement fields as indicated in Table 1, except where a/h=4 and $SR = 10^5$, in which case the transverse elastic deformation for such a thick plate with very soft core is too significant to be neglected. Since the proposed model is intended for the analysis of thin-to-moderately thick plates and shells, the neglect of the through-thickness variation in the transverse displacement still yields good results within the scope of interest.

The through-thickness variations of the planar stress $\bar{\sigma}_x$ (a/2, b/2) for the cases where a/h=100 (thin plate) and $FCSR = 10, 10^5$ are depicted in Figure 19, which highlight the accuracy of the SS-MITC9 model for a wide range of FCSR values. The noticeable deviation of the EDZ1 curve in Figure 19.b indicates the inaccuracy of Murakami's function in capturing the zigzag effect. This deviation is alleviated with the use of higher-order EDZ models.

Figure 20 shows the through-thickness distributions of the non-dimensional transverse shear stress $\bar{\sigma}_{xz}$ (0, b/2) for the cases where a/h=4 (thick plate) and $FCSR = 10, 10^5$. Clearly, the continuous transverse shear stress predicted by the EDZ4 model posts a close approximation of the elasticity solution. On the other hand, the SS-MITC9 model, which assumes a piecewise linear-constant-linear transverse shear strain pattern, provides an accurate prediction of transverse shear stresses in the core, though discrepancies arise in the face sheets. As stated before, the assumed piecewise linear-constant-linear distribution of transverse shear stresses leads to the transverse shear stress distribution in the face sheets not being accurately predicted for a large FCSR. However, this has negligible influence on the results owing to the fact that it is the core that offers the dominant contribution to the overall transverse shear strain energy. With further manipulation, the through-thickness variation of the transverse shear strain at (0, b/2) for the case a/h=4 and FCSR=10 can be obtained for each model, as depicted in Figure 21, with the non-dimensional transverse shear strain

expressed as $\overline{\gamma}_{xz} = \frac{E^{(2)}}{E^{(k)}}\overline{\sigma}_{xz}$. Clearly, the transverse shear strains in the face sheets are much smaller than the strain in the soft layer, which indicates negligible influence of the stiff layers on the overall transverse shear strain energy.

The advantage of the SS-MITC9 element is highlighted in this asymmetrically laminated sandwich plate example. The proposed sandwich shell model surpasses EDZ1 in terms of both accuracy and efficiency, and is even more accurate than EDZ models with higher-order z expansions in the analysis of thin-to-moderately thick asymmetrically laminated sandwich plates with a wide range of FCSRs.

6.4 Circular plate under uniform pressure

The geometrically nonlinear response of a circular sandwich plate is considered here, where the plate is fully clamped along its edge and is subjected to a uniformly distributed transverse loading p, as shown in Figure 22. The geometric and material parameters are given by $R = 20$, $h = 0.5$, $E^{(1)} = E^{(3)} = 1.0\times10^{7}$, $E^{(2)} = 3750$, and $\nu^{(1)} = \nu^{(2)} = \nu^{(3)} = 0.25$. A symmetric lay-up is first considered, where $h_1 = h_3 = 0.025$ and $h_2 = 0.45$. Due to symmetry, a quarter of the circular plate is modelled with a mesh of 9-noded sandwich shell elements, which provides a convergent solution. The mesh is depicted in Figure 23, where the quarter model is divided into three sections, with each section discretised into 6×6 SS-MITC9 elements. The curvilinear shell system is chosen by using the definition shown in Figure 10 with the reference vector **n** aligned with the x-axis. By restraining all the additional DOFs, a FSDT-MITC9 solution is also available. On the other hand, a 'EDZ1*' formulation, which adds the MZZF to planar displacements of the Reissner-Mindlin formulation and employs the assumed piecewise linear-constant-linear distribution of transverse shear strains, is also implemented with the 9-noded co-rotational element for comparison. It is worth noting that the only difference between the EDZ1*-MITC9 model and the SS-MITC9 model is the employed zigzag function, which facilities the comparison between both additional displacement variables in modelling the considered laminations. The load-deflection curves at the plate centre O with the considered models are depicted in Figure 24, along with the series solution by Smith [42] and the solution with axisymmetric sandwich shell elements by

Sharifi and Popov [43] (eight equally spaced 5-noded axisymmetric elements). As is expected, the SS-MITC9 and the EDZ1*-MITC9 results are identical for the symmetric lay-up, both of which agree with the series solution.

An asymmetric lay-up is also considered, where the thicknesses of the layers are given as $h_1 = 0.05$, $h_2 = 0.35$, and $h_3 = 0.1$. The reference solution is taken from the results with a fine 3D model using a standard 20-noded quadratic brick element [44], denoted as 'BK20', where in the planar surface each of the three sections are meshed with 24×24 of the BK20 elements, and in the through-thickness direction an element size of 0.025 is employed. The SS-MITC9, EDZ1*-MITC9 and FSDT results with the same mesh as Figure 23 are given in Figure 25, compared with the solution from the 3D elasticity model of the BK20 element. The SS-MITC9 element still shows high accuracy in predicting the large displacement response of the asymmetrically laminated sandwich plate, but the EDZ1*-MITC9 results are as inaccurate as the FSDT-MITC9 solution owing to the inadequacy of Murakami's zigzag function in capturing the real zigzag mode, hence requiring higher-order Taylor expansions with more additional displacement variables for improved estimation.

.

6.5 Clamped cylindrical sandwich shell under point load

This is another large displacement problem, where a sandwich cylindrical shell, clamped along its two straight edges, is loaded with a concentrated transverse force at its centre, as is depicted in Figure 26. The deflected plate configuration is depicted in Figure 27. The core and the face sheets are made of isotropic materials. The mechanical properties of the core are: $E^{(2)} = 7.2\times10^7$, and $\nu^{(2)} = 0.22$. The Young's modulus and shear modulus of the face sheets are obtained by multiplying those of the core with a FCSR=1000. The thicknesses of the layers are $h_1 = h_3 = 0.05$ and $h_2 = 0.01$. A quarter of the structure is modelled due to symmetry, in which uniform 4×4 and 8×8 meshes of the SS-MITC9 element are employed. In this model, the shell system can be obtained according to the approach illustrated in Figure 10 with the reference vector **n** aligned with the axis of revolution, in which case the r- and s-axes orient along the circumferential and the longitudinal directions, respectively.

The equilibrium paths of the central deflection for both meshes are depicted in Figure 28, from which it is evident that the coarser 4×4 mesh matches well with the finer mesh. Also depicted in the figure are the results from a 4×4 FSDT-MITC9 model and a 32×32×6 solid model using the BK20 element [44], where two elements are employed for each layer. There is a significant deviation of the FSDT-MITC9 solution from the others, which indicates that the sectional warping cannot be ignored. Evidently, the equilibrium path of a coarse 4×4 mesh of the SS-MITC9 element matches well with the solid model, which confirms the effectiveness of the proposed element.

6.6 Sandwich annular plate under end shear

A sandwich annular plate, fully clamped at one end, is subjected to a uniformly distributed transverse shear force at the other end, as is shown in Figure 29. The fibre direction of each layer is at a planar angle $\alpha^{(k)}$ from the circumferential direction of the annular plate. The plate dimensions are given as: $R_1 = 6$, $R_2 = 10$, $h = 0.045$, and $h_1 = h_2 = h_3 = 0.015$. The mechanical properties of the core are: $E_1^{(2)} = 2.0\times10^6$, $E_2^{(2)} = 6.0\times10^5$, $G_{12}^{(2)} = G_{13}^{(2)} = 3.0\times10^5$, $G_{23}^{(2)} = 2.4\times10^5$, and $\nu_{12}^{(2)} = 0.3$. The Young's modulus and shear modulus of the face sheets are obtained by multiplying those of the core with a FCSR=1000.

The shell system is obtained according to the approach illustrated in Figure 11 with the reference point O located at the origin of the global system (Figure 29) such that the r- and s-axes orient along the circumferential and the radial directions, respectively. The deflected shape of the plate is shown in Figure 30. It is important to note that the element-specific definition of the shell system would yield noticeable inaccuracy in this problem if the discretisation along the circumferential direction is very coarse. Figure 31 depicts the load-displacement curves in z direction at point A and B for two uniform meshes of the whole plate (32×4 and 64×4) using the SS-MITC9 element for a symmetric lay-up ($h_1 = h_2 = h_3 = 0.015$) with a (0°/0°/0°) stacking scheme. Also presented are results from a 96×10×6 mesh of the degenerated shell element SOLSH190 in the finite element software package, ANSYS [45], where each individual sheet is modelled with 2 layers of elements through the thickness to represent the local zigzag effect. Clearly, results from both meshes

of the SS-MITC9 element agree well with the SOLSH190 solution, indicating negligible inaccuracy resulting from the element-specific definition of the shell system with the coarser 32×4 mesh. Figures 32-33 depict the results from a 32×4 mesh of the SS-MITC9, EDZ1*-MITC9, and FSDT-MITC9 element for respectively a symmetric lay-up ($h_1 = h_2 = h_3 = 0.015$) and an asymmetric lay-up ($h_1 = 0.02$, $h_2 = 0.015$, and $h_3 = 0.01$), both of which employ a (0°/0°/0°) stacking scheme. Still, the results of the SS-MITC9 element are identical to the EDZ1*-MITC9 solution for the symmetric lay-up while surpass those of the EDZ1*-MITC9 element for the asymmetric lay-up.

Figure 34 depicts the results from a 32×4 mesh of the SS-MITC9 for symmetric lay-ups ($h_1 = h_2 = h_3 = 0.015$) with various fibre orientations, where the coincident plots of the SS-MITC9 and SOLSH190 meshes confirm the accuracy and effectiveness of the SS-MITC9 element in solving large displacement problems with arbitrary fibre orientations.

7 CONCLUSIONS

This paper presents a sandwich shell modelling approach for the nonlinear analysis of thin to moderately thick sandwich plates and shells with a soft core, which is instantiated with a 9-noded co-rotational shell element for large displacement analysis of sandwich shell structures.

The sandwich structure, as a special lamination, is characterised by a significantly large stiffness mismatch through the thickness. Under transverse loading, the face sheets have almost identical rotations of the normal. Furthermore, the transverse shear strain exhibits a near constant through-thickness distribution in each of the soft layers, while it is much smaller in the face sheets. Based on these characteristics, a simple yet effective sandwich model is proposed, in which the zigzag effect of planar displacements is taken into account by adding to the Reissner-Mindlin formulation a zigzag displacement field specific to sandwich structures. For sandwich structures with symmetric cross-sections, the proposed zigzag function is equivalent to Murakami's zigzag function, whereas for asymmetrically laminated applications, the proposed zigzag function achieves superior accuracy in capturing the local structural behaviour. In addition, a piecewise linear-constant-linear distribution of the transverse shear strain is assumed in the thickness direction, which leads to an effective

representation of the real distribution without imposing computational demanding stress constrains at laminar interfaces. A 1D beam problem is used to illustrate the effectiveness and efficiency of the proposed sandwich model via the comparison against other models for various FCSR values in both symmetrically and asymmetrically laminated scenarios.

The proposed sandwich model developed for shallow shell finite elements can be applied in large displacement analysis with the use of a co-rotational approach. In this respect, to eliminate the need for co-rotational transformations for the additional zigzag displacement parameters, a 2D curvilinear shell system is proposed in this paper for the direct definition of these parameters, such that a simple and fixed transformation of these additional parameters to their counterparts in the local element system holds throughout the analysis.

The application of the proposed sandwich shell modelling approach is illustrated for a 9-noded co-rotational shell element, which employs a bisector definition of the co-rotational system, and utilises the MITC9 strain mapping approach in the local system to address locking. Linear and geometrically nonlinear numerical examples are finally solved with the proposed sandwich shell formulation, where excellent accuracy is generally achieved in comparison with elasticity solutions, and superior performance is typically demonstrated compared to existing models for asymmetric lay-ups.

REFERENCES

[1] Whitney JM, Pagano NJ. Shear deformation in heterogeneous anisotropic plates. *Journal of Applied Mechanics* 1970; **37**(4): 1031-1036.

[2] Pandya B, Kant T. Higher-order shear deformable theories for flexure of sandwich plates-finite element evaluations. *International Journal of Solids and Structures* 1988;**24**(12):1267-1286.

[3] Reddy J, Liu C. A higher-order shear deformation theory of laminated elastic shells. *International Journal of Engineering Science* 1985;**23**(3):319-330.

[4] Carrera E. Theories and finite elements for multilayered plates and shells: a unified compact formulation with numerical assessment and benchmarking. *Archives of Computational Methods in Engineering* 2003; **10**(3): 215-296.

[5] Reddy JN. On refined computational models of composite laminates. *International Journal for Numerical Methods in Engineering* 1989; **27(2)**:362-382.

[6] Reddy JN. Mechanics of laminated composite plates and shells: Theory and analysis. CRC press; 2003.

[7] Robbins D, Reddy J. Modelling of thick composites using a layerwise laminate theory. *International Journal for Numerical Methods in Engineering* 1993;**36**(4):655-677.

[8] Pandit MK, Sheikh AH, Singh BN. An improved higher order zigzag theory for the static analysis of laminated sandwich plate with soft core. *Finite Elements in Analysis and Design* 2008;**44**(9):602-610.

[9] Chalak HD, Chakrabarti, A, Iqbal MA, Sheikh AH. An improved C_0 FE model for the analysis of laminated sandwich plate with soft core. *Finite Elements in Analysis and Design* 2012; **56**:20-31.

[10] Murakami H. Laminated composite plate theory with improved in-plane responses. *Journal of Applied Mechanics* 1986;**53**(3): 661-666.

[11] Carrera E. An assessment of mixed and classical theories on global and local response of multilayered orthotropic plates. *Composite structures* 2000; **50**(2): 183-198.

[12] Carrera E. On the use of the Murakami's zig-zag function in the modeling of layered plates and shells. *Computers & Structures* 2004; **82**(7): 541-554.

[13] Carrera E. C0 Reissner-Mindlin multilayered plate elements including Zigzag and Interlaminar stress continuity. *International Journal for Numerical Methods in Engineering* 1996;**39**(11):1797-1820.

[14] Brank B, Carrera E. Multilayered shell finite element with interlaminar continuous shear stresses: A refinement of the Reissner-Mindlin formulation. *International Journal for Numerical Methods in Engineering* 2000;**48**(6):843-874.

[15] Brischetto S, Carrera E, Demasi L. Improved response of unsymmetrically laminated sandwich plates by using zig-zag functions. *Journal of Sandwich Structures and Materials*, 2009; **11**(2-3): 257-267.

[16] Carrera E. Developments, ideas, and evaluations based upon Reissner's Mixed Variational Theorem in the modeling of multilayered plates and shells. *Applied Mechanics Reviews 2001*; **54**(4): 301-329.

[17] Carrera E. A refined multilayered finite-element model applied to linear and non-linear analysis of sandwich plates. *Composites Science and Technology* 1998; **58**(10): 1553-1569.

[18] Carrera E, Krause H. An investigation of non-linear dynamics of multilayered plates accounting for C 0 z requirements. *Computers & Structures* 1998; **69**(4): 473-486.

[19] Carrera E, Parisch H. An evaluation of geometrical nonlinear effects of thin and moderately thick multilayered composite shells. *Composite Structures* 1997; **40**(1): 11-24.

[20] Carrera E. An improved Reissner-Mindlin-type model for the electromechanical analysis of multilayered plates including piezo-layers. *Journal of Intelligent Material Systems and Structures* 1997; **8**(3): 232-248.

[21] Reissner E. The effect of transverse shear deformation on the bending of elastic plates. *Journal of Applied Mechanics* 1945; **12**(2): 69-77.

[22] Mindlin RD. Influence of rotary inertia and shear on flexural motions of isotropic elastic plates. *Journal of Applied Mechanics* 1951; **18**: 31-38.

[23] Bathe KJ. Finite element procedures. Prentice Hall, 1996, 2nd edition KJ Bathe, Watertown, MA, 2014.

[24] Sussman T, Bathe KJ. 3D-shell elements for structures in large strains. *Computers & Structures 2013*; **122**: 2-12.

[25] Izzuddin BA. An enhanced co-rotational approach for large displacement analysis of plates. *International Journal for Numerical Methods in Engineering* 2005;**64**(10):1350-1374.

[26] Crisfield MA, Moita GF. A unified co-rotational framework for solids, shells and beams. *International Journal of Solids and Structures* 1996; **33**(20):2969–2992.

[27] Li Z, Izzuddin BA, Vu-Quoc L. A 9-node co-rotational quadrilateral shell element. *Computational Mechanics* 2008;**42**(6):873-884.

[28] Izzuddin BA, Liang Y. Bisector and zero-macrospin co-rotational systems for shell elements. *International Journal for Numerical Methods in Engineering* 2015.

[29] Bathe KJ, Dvorkin EN. A formulation of general shell elements—the use of mixed interpolation of tensorial components. *International Journal for Numerical Methods in Engineering* 1986; **22**(3):697-722.

[30] Bucalem ML, Bathe KJ. Higher-order MITC general shell elements. *International Journal for Numerical Methods in Engineering* 1993; **36**(21):3729-3754.

[31] Lee PS, Bathe KJ. The quadratic MITC plate and MITC shell elements in plate bending. *Advances in Engineering Software* 2010; **41**(5):712-728.

[32] Bathe KJ, Lee PS, Hiller JF. Towards improving the MITC9 shell element. Computers & Structures 2003; 81(8):477-489.

[33] Wisniewski K, Panasz P. Two improvements in formulation of nine-node element MITC9. *International Journal for Numerical Methods in Engineering* 2013; **93**(6):612-634.

[34] Hu H, Belouettar S, Potier-Ferry M. Review and assessment of various theories for modeling sandwich composites. *Composite Structures* 2008; **84**(3): 282-292.

[35] Izzuddin BA. Nonlinear dynamic analysis of framed structures, PhD Thesis, Imperial College, University of London, 1991.

[36] Pagano N. Exact solutions for rectangular bidirectional composites and sandwich plates. *Journal of Composite Materials* 1970;**4**(1):20-34.

[37] Balah M, Al-Ghamedy HN. Finite element formulation of a third order laminated finite rotation shell element. *Computers & Structures* 2002;**80**(26):1975-1990.

[38] Thai CH, Ferreira A, Carrera E, Nguyen-Xuan H. Isogeometric analysis of laminated composite and sandwich plates using a layerwise deformation theory. *Composite Structures* 2013;**104**:196-214.

[39] Srinivas S, Rao A. Bending, vibration and buckling of simply supported thick orthotropic rectangular plates and laminates. *International Journal of Solids and Structures* 1970;**6**(11):1463-1481.

[40] Ferreira A, Fasshauer G, Batra R, Rodrigues J. Static deformations and vibration analysis of composite and sandwich plates using a layerwise theory and RBF-PS discretizations with optimal shape parameter. *Composite structures* 2008;**86**(4):328-343.

[41] Demasi L. 2D, quasi 3D and 3D exact solutions for bending of thick and thin sandwich plates. *Journal of Sandwich Structures and Materials* 2008; **10**(4): 271-310.

[42] Smith CV. Large deflections of circular sandwich plates. *AIAA Journal* 1968; **6**(4): 721-723.

[43] Sharifi P, Popov EP. Nonlinear finite element analysis of sandwich shells of revolution. *AIAA Journal* 1973; **11**(5): 715-722.

[44] Zeinkiewicz OC, Taylor RL, Zhu, JZ. *The finite element method: its basis and fundamentals.*2005.

[45] ANSYS, ANSYS user manual, Version 15.0, 2013.

APPENDIX A: PARAMETERS OF ZIGZAG FUNCTIONS

Explicit expressions of $\hat{a}_i^{(k)}$ and $\hat{b}_i^{(k)}$ (i=3,4) in (1)-(2) are given by:

$$\hat{a}_3^{(1)} = \frac{1}{h_1} - \frac{(h_1 - h_3)(h_1 + 3h_2 + h_3)}{(h_1 + h_2 + h_3)^3} \tag{A1}$$

$$\hat{a}_3^{(2)} = -\frac{(h_1 - h_3)(h_1 + 3h_2 + h_3)}{(h_1 + h_2 + h_3)^3} \tag{A2}$$

$$\hat{a}_3^{(3)} = -\frac{1}{h_3} - \frac{(h_1 - h_3)(h_1 + 3h_2 + h_3)}{(h_1 + h_2 + h_3)^3} \tag{A3}$$

$$\hat{b}_3^{(1)} = \hat{b}_3^{(3)} = \frac{h_1 h_3 + (h_2 + h_3)^2}{2h_1(h_1 + h_2 + h_3)} \tag{A4}$$

$$\hat{b}_3^{(2)} = \frac{h_1 + h_3}{2(h_1 + h_2 + h_3)} \tag{A5}$$

$$\hat{a}_4^{(1)} = \hat{a}_4^{(3)} = -\frac{h_2^2 + 3h_1h_2 + 6h_1h_3 + 3h_2h_3}{(h_1 + h_2 + h_3)^3} \tag{A6}$$

$$\hat{a}_4^{(2)} = \frac{1}{h_2} - \frac{h_2^2 + 3h_1h_2 + 6h_1h_3 + 3h_2h_3}{(h_1 + h_2 + h_3)^3} \tag{A7}$$

$$\hat{b}_4^{(1)} = -\frac{h_2 + 2h_3}{2(h_1 + h_2 + h_3)} \tag{A8}$$

$$\hat{b}_4^{(2)} = -\frac{h_1^2 + 2h_3^2}{2h_2(h_1 + h_2 + h_3)} \tag{A9}$$

$$\hat{b}_4^{(3)} = -\frac{2h_1 + h_2}{2(h_1 + h_2 + h_3)} \tag{A10}$$

For symmetric cross-sections, the above equations are simplified to:

$$\hat{a}_3^{(1)} = -\hat{a}_3^{(3)} = \frac{1}{h_1}, \quad \hat{a}_3^{(2)} = 0 \tag{A11}$$

$$\hat{b}_3^{(1)} = \hat{b}_3^{(3)} = \frac{2h_1^2 + h_2^2 + 2h_1h_2}{2h_1(2h_1 + h_2)}, \quad \hat{b}_3^{(2)} = \frac{h_1}{2h_1 + h_2} \tag{A12}$$

$$\hat{a}_4^{(1)} = \hat{a}_4^{(3)} = -\frac{6h_1^2 + h_2^2 + 6h_1h_2}{(2h_1 + h_2)^3}, \quad \hat{a}_4^{(2)} = \frac{1}{h_2} - \frac{6h_1^2 + h_2^2 + 6h_1h_2}{(2h_1 + h_2)^3} \tag{A13}$$

$$\hat{b}_4^{(1)} = -\hat{b}_4^{(3)} = -\frac{1}{2}, \quad \hat{b}_4^{(2)} = 0 \tag{A14}$$

APPENDIX B: GLOBAL-TO-LOCAL DISPLACEMENT TRANSFORMATIONS

A bisector definition of the co-rotational system, previously proposed for quadrilateral shell elements with varying orders and types with the use of four corner nodal coordinates only [25], is adopted. The triad $(\mathbf{c}_x, \mathbf{c}_y, \mathbf{c}_z)$, which describes the current orientation of the local coordinate system relative to the global system, is simply obtained as follows [25]:

$$\mathbf{c}_x = \frac{\mathbf{c}_{13} - \mathbf{c}_{24}}{\left|\mathbf{c}_{13} - \mathbf{c}_{24}\right|}, \quad \mathbf{c}_y = \frac{\mathbf{c}_{13} + \mathbf{c}_{24}}{\left|\mathbf{c}_{13} + \mathbf{c}_{24}\right|}, \quad \mathbf{c}_z = \mathbf{c}_x \times \mathbf{c}_y \tag{B1}$$

with:

$$\mathbf{c}_{ij} = \frac{\mathbf{v}_{ij}}{\left|\mathbf{v}_{ij}\right|}, \quad \mathbf{v}_{ij} = \mathbf{v}_{ij}^o + \mathbf{d}_j - \mathbf{d}_i \tag{B2}$$

where $\mathbf{v}_{ij}^o$ is the vector connecting node *i* to node *j* in the initial element configuration, and $\mathbf{d}_i = \left\langle u_{X,i}, u_{Y,i}, u_{Z,i} \right\rangle^T$ represents the global translational displacements of node *i*.

The transformation between global and local translational displacements can be expressed as [28]:

$$\mathbf{t}_i = \mathbf{R}\mathbf{d}_i + \left(\mathbf{R} - \mathbf{R}^o\right)\mathbf{v}_{io}^o \quad (i = 1 \to 9) \tag{B3}$$

where $\mathbf{t}_i = \left\langle u_{x0,i}, u_{y0,i}, u_{z0,i} \right\rangle^T$ represents the local translational displacements of node *i*; $\mathbf{R}^o$ and $\mathbf{R}$ are the orientation matrices of the local co-rotational system in the initial and current configurations, respectively, defined as:

$$\mathbf{R}^o = \left[\mathbf{c}_x^o \;\; \mathbf{c}_y^o \;\; \mathbf{c}_z^o\right]^T, \quad \mathbf{R} = \left[\mathbf{c}_x \;\; \mathbf{c}_y \;\; \mathbf{c}_z\right]^T \tag{B4}$$

and $\mathbf{v}_{io}^o$ is a vector describing the initial position of node *i* relative to a reference point *o*, which is selected at the internal node for the 9-noded shell element. It should be noted that choice of the reference point does not impact on accuracy, since a change in location of *o* merely results in the addition of an increment of rigid body translations to which the local element formulation should be insensitive.

The transformation between global and local rotations is [25,28]:

$$\bar{\mathbf{r}}_i = \bar{\mathbf{R}}\,\mathbf{n}_i, \quad \bar{\mathbf{R}} = \left[\mathbf{c}_x \;\; \mathbf{c}_y\right]^T \quad (i = 1 \to 9) \tag{B5}$$

where $\overline{\mathbf{r}}_i = \left\langle \theta_{x,i}, \theta_{y,i} \right\rangle^T$ represents the two rotations at node *i* in the local x-z and y-z planes, respectively; $\mathbf{n}_i$ is the normal vector at node *i*.

Table 1: Evaluation of different models for a symmetrically laminated sandwich beam with various FCSRs.

Results		Reference value	FSDT	HSDT [34]	IC-ZZT [34]	ID-ZZT [34]	Present
FCSR=10^4	$\bar{u}_z$	-2.24E-04	-4.71E-05	-4.72E-05	-2.23E-04	-2.23E-04	-2.23E-04
	$\bar{\sigma}_x$	-6.90E+05	-3.89E+05	-3.89E+05	-6.90E+05	-6.90E+05	-6.90E+05
	$\bar{\sigma}_{xz}$	-4.64E+03	-7.50E-01	-1.77E+00	-4.63E+03	-4.63E+03	-4.63E+03
FCSR=10^3	$\bar{u}_z$	-7.32E-05	-4.71E-05	-4.72E-05	-7.31E-05	-7.31E-05	-7.32E-05
	$\bar{\sigma}_x$	-3.98E+05	-3.89E+05	-3.89E+05	-3.98E+05	-3.98E+05	-3.98E+05
	$\bar{\sigma}_{xz}$	-6.79E+03	-7.50E+00	-1.77E+01	-6.76E+03	-6.76E+03	-6.76E+03
FCSR=10^2	$\bar{u}_z$	-4.99E-05	-4.71E-05	-4.71E-05	-4.99E-05	-4.99E-05	-4.99E-05
	$\bar{\sigma}_x$	-3.89E+05	-3.89E+05	-3.89E+05	-3.89E+05	-3.89E+05	-3.89E+05
	$\bar{\sigma}_{xz}$	-6.93E+03	-7.46E+01	-1.75E+02	-6.93E+03	-6.93E+03	-6.93E+03
FCSR=10^1	$\bar{u}_z$	-4.72E-05	-4.69E-05	-4.70E-05	-4.72E-05	-4.72E-05	-4.72E-05
	$\bar{\sigma}_x$	-3.88E+05	-3.88E+05	-3.88E+05	-3.88E+05	-3.88E+05	-3.88E+05
	$\bar{\sigma}_{xz}$	-7.00E+03	-7.14E+02	-1.56E+03	-7.01E+03	-6.95E+03	-6.95E+03
FCSR=10^0	$\bar{u}_z$	-4.53E-05	-4.53E-05	-4.53E-05	-4.53E-05	-4.53E-05	-4.53E-05
	$\bar{\sigma}_x$	-3.75E+05	-3.75E+05	-3.75E+05	-3.75E+05	-3.75E+05	-3.75E+05
	$\bar{\sigma}_{xz}$	-7.64E+03	-5.00E+03	-7.50E+03	-7.73E+03	-7.22E-03	-7.22E+03

Table 2: Evaluation of different models for an asymmetrically laminated sandwich beam with various FCSRs.

Results		Case 1 ($h_3/h_1 = 2$, $h_2/h_1 = 7$)				Case 2 ($h_3/h_1 = 2$, $h_2/h_1 = 2$)			
		Reference value	Relative Error			Reference value	Relative Error		
			Present	MZZF1	MZZF 2		Present	MZZF 1	MZZF 2
FCSR=10^4	$\bar{u}_z$	-4.43E-04	0.00%	82.23%	1.13%	-2.39E-04	0.00%	77.54%	1.57%
	$\bar{\sigma}_x$	-6.38E+05	0.00%	23.26%	0.04%	-7.92E+05	0.00%	52.08%	3.98%
	$\bar{\sigma}_{xz}$	-5.47E+03	0.00%	99.61%	4.95%	-4.31E+03	0.00%	99.66%	3.09%
FCSR=10^3	$\bar{u}_z$	-1.19E-04	0.00%	33.85%	0.53%	-8.08E-05	0.00%	33.62%	0.05%
	$\bar{\sigma}_x$	-4.90E+05	0.00%	0.02%	0.00%	-3.92E+05	0.01%	3.05%	0.24%
	$\bar{\sigma}_{xz}$	-5.79E+03	0.01%	96.47%	5.07%	-6.37E+03	0.00%	97.76%	3.06%
FCSR=10^2	$\bar{u}_z$	-8.08E-05	0.00%	3.90%	0.09%	-5.59E-05	0.00%	4.47%	0.01%
	$\bar{\sigma}_x$	-4.90E+05	0.00%	0.00%	0.00%	-3.80E+05	0.00%	0.00%	0.00%
	$\bar{\sigma}_{xz}$	-5.80E+03	0.07%	73.13%	5.08%	-6.55E+03	0.02%	81.54%	3.02%
FCSR=10^1	$\bar{u}_z$	-7.12E-05	0.00%	0.12%	0.01%	-5.21E-05	0.00%	0.16%	0.00%
	$\bar{\sigma}_x$	-4.86E+05	0.00%	0.00%	0.00%	-3.80E+05	0.00%	0.00%	0.00%
	$\bar{\sigma}_{xz}$	-5.89E+03	0.75%	20.40%	4.87%	-6.58E+03	0.28%	27.69%	2.64%
FCSR=10^0	$\bar{u}_z$	-4.53E-05	0.00%	0.00%	0.00%	-4.53E-05	0.00%	0.00%	0.00%
	$\bar{\sigma}_x$	-3.75E+05	0.00%	0.00%	0.00%	-3.75E+05	0.00%	0.00%	0.00%
	$\bar{\sigma}_{xz}$	-6.65E+03	6.83%	0.88%	0.83%	-7.04E+03	3.34%	0.75%	0.56%

Table 3: Dimensionless deflection and stresses of a sandwich plate with various (a/h) ratios.

a/h	Model	$\bar{u}_z$	$\bar{\sigma}_x$	$\bar{\sigma}_y$	$\bar{\sigma}_{xz}$	$\bar{\sigma}_{yz}$	$\bar{\sigma}_{xy}$
100	FSDT [2]	0.883	1.104	0.0546	0.2875	0.0270	-0.0435
	TSDT [37]	0.8903	1.0958	0.0548	0.3741	0.0342	-0.0436
	LWT [38]	0.8924	1.0975	0.0549	0.3234	0.0291	-0.0437
	ZZT [8]	0.8917	1.1093	0.0547	0.3412	0.0324	-0.0434
	SS-MITC9	0.8923	1.1009	0.0551	0.3244	0.0292	-0.0439
	Elasticity [36]	0.8923	1.0980	0.0550	0.3240	0.0297	-0.0437
50	LWT [38]	0.9348	1.0989	0.0569	0.3225	0.0299	-0.0446
	ZZT [8]	0.9341	1.0948	0.0566	0.3403	0.0333	-0.0445
	SS-MITC9	0.9348	1.1022	0.0570	0.3236	0.0300	-0.0449
	Elasticity [36]	0.9348	1.0990	0.0569	0.3230	0.0306	-0.0446
20	LWT [38]	1.2262	1.1090	0.0697	0.3168	0.0352	-0.0511
	ZZT [8]	1.2254	1.1055	0.0694	0.3342	0.0392	-0.0509
	SS-MITC9	1.2264	1.1115	0.0699	0.3178	0.0354	-0.0514
	Elasticity [36]	1.2264	1.1100	0.0700	0.3170	0.0361	-0.0511
10	FSDT [2]	1.557	1.062	0.0806	0.2779	0.0364	-0.0553
	TSDT [37]	2.0830	1.1470	0.1040	0.3489	0.0578	-0.0687
	LWT [38]	2.2011	1.1497	0.1090	0.2993	0.0513	-0.0712
	ZZT [8]	2.2002	1.1483	0.1086	0.3158	0.0570	-0.0709
	SS-MITC9	2.2004	1.1495	0.1093	0.3003	0.0515	-0.0716
	Elasticity [36]	2.2004	1.1530	0.1104	0.3000	0.0527	-0.0707

Table 4: Dimensionless deflection and stresses of a sandwich plate with various FCSRs.

FCSR	Model	$\bar{u}_z$	$\bar{\sigma}_x^1$	$\bar{\sigma}_x^2$	$\bar{\sigma}_x^3$	$\bar{\sigma}_y^1$	$\bar{\sigma}_y^2$	$\bar{\sigma}_y^3$	$\bar{\sigma}_{xz}$
5	FSDT [2]	236.10	61.87	49.50	9.899	36.65	29.32	5.864	3.313
	HSDT [2]	256.13	62.38	46.91	9.382	38.93	30.33	6.065	3.089
	LWT [40]	258.180	60.063	46.393	9.279	38.364	30.029	6.006	4.095
	SS-MITC9	258.958	60.302	46.604	9.321	38.523	30.155	6.031	4.132
	Elasticity [39]	258.970	60.353	46.623	9.340	38.491	30.097	6.161	4.364
10	FSDT [2]	131.095	67.80	54.24	4.424	40.10	32.08	3.208	3.152
	HSDT [2]	152.330	64.65	51.31	5.131	42.83	33.97	3.397	3.147
	LWT [40]	158.912	64.993	48.601	4.860	43.491	33.409	3.341	3.980
	SS-MITC9	159.480	65.281	48.836	4.884	43.682	33.554	3.355	4.030
	Elasticity [39]	159.380	65.332	48.857	4.903	43.566	33.413	3.500	4.096
15	FSDT [2]	90.85	70.04	56.03	3.753	41.39	33.11	2.208	3.091
	HSDT [2]	110.43	66.62	51.97	3.465	44.92	35.41	2.361	3.035
	LWT [40]	121.347	66.436	48.010	3.201	46.385	34.965	2.331	3.902
	SS-MITC9	121.821	66.727	48.273	3.218	46.582	35.138	2.343	3.958
	Elasticity [39]	121.720	66.787	48.299	3.238	46.424	34.955	2.494	3.964

Table 5: Number of displacement fields for the considered sandwich plate models.

Model	Number of displacement variables
SS-MITC9	7
EDZ1 [15]	9
EDZ4 [15]	18
EDZ5 [15]	21
EDZ6 [15]	24
EDZ7 [15]	27

Table 6: Relative accuracy of various models in the evaluation of central deflection.

a/h	Model	FCSR			
		10		10^5	
		$\bar{u}_z$	Relative error (%)	$\bar{u}_z$	Relative error (%)
4	Elasticity [41]	3.01123	-	0.013159	-
	SS-MITC9	2.98319	0.93	0.011907	9.51
	FSDT-MITC9	1.58218	47.46	0.000180	98.63
	EDZ1 [15]	2.34412	22.15	0.000837	93.64
	EDZ4 [15]	2.97886	1.07	0.012629	4.03
	EDZ5 [15]	2.98737	0.79	0.013041	0.90
	EDZ6 [15]	2.99508	0.54	0.013116	0.33
	EDZ7 [15]	2.99670	0.48	0.013136	0.17
100	Elasticity [41]	1.51021	-	0.002089	-
	SS-MITC9	1.51027	0.00	0.002089	0.01
	FSDT-MITC9	1.10845	26.60	0.000120	94.26
	EDZ1 [15]	1.15866	23.28	0.000163	92.18
	EDZ4 [15]	1.51017	0.00	0.001163	44.34
	EDZ5 [15]	1.51018	0.00	0.001784	14.61
	EDZ6 [15]	1.51019	0.00	0.001975	5.48
	EDZ7 [15]	1.51019	0.00	0.002021	3.30

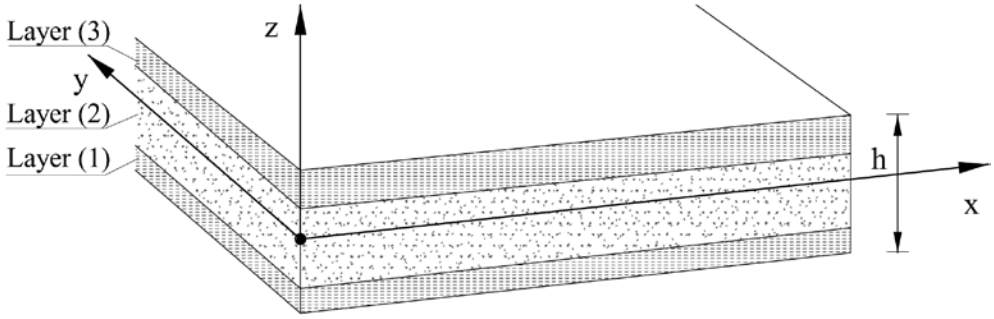


Figure 1: Three-layered sandwich plate and local coordinate system.

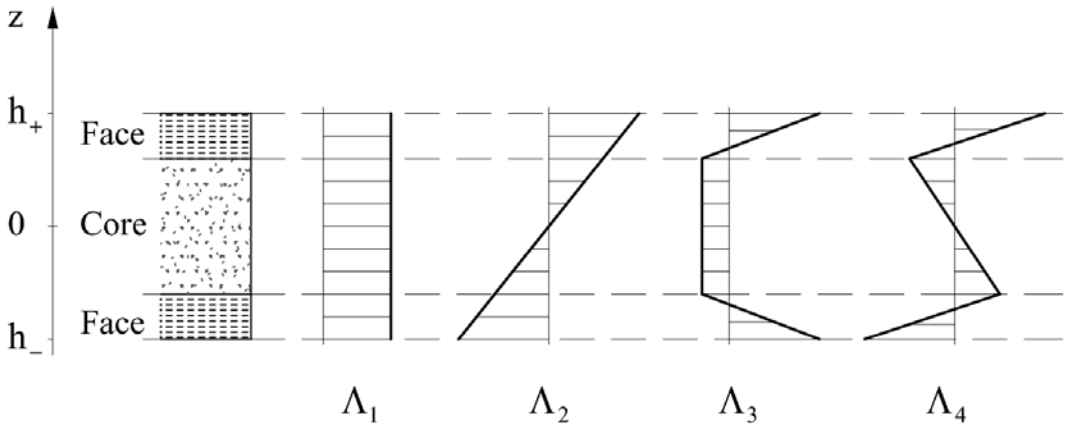
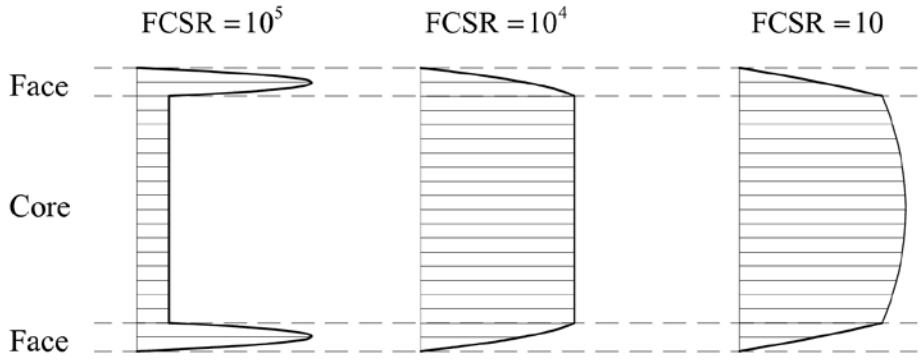
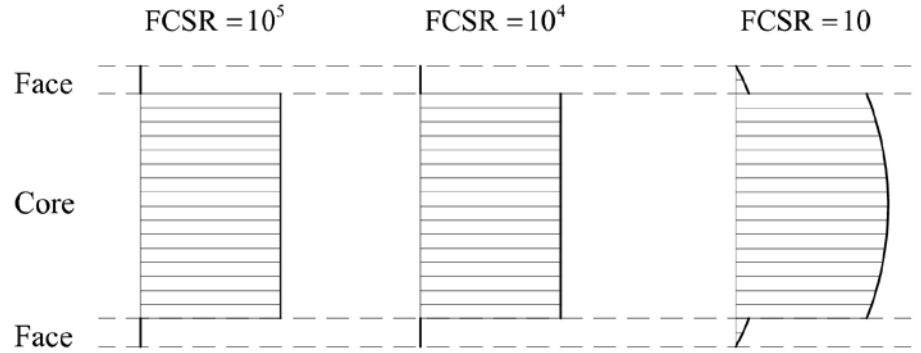


Figure 2: Four through-thickness displacement modes for sandwich plate.



a. transverse shear stress



b. transverse shear strain

Figure 3: Through-thickness distribution of transverse shear stress/strain with various FCSRs.

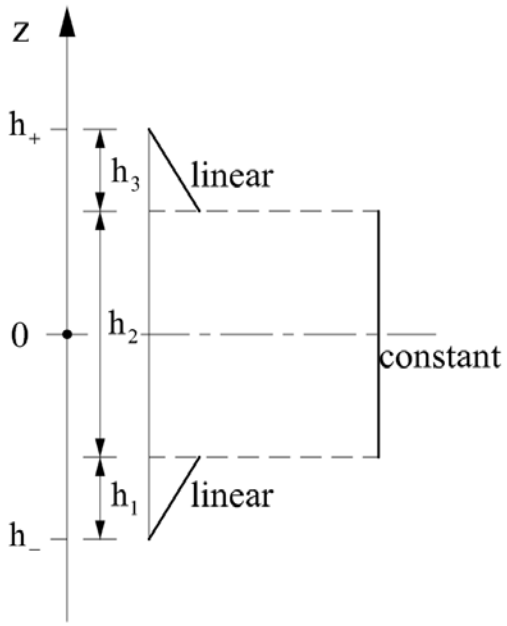


Figure 4: Assumed through-thickness distribution of transverse shear strain.

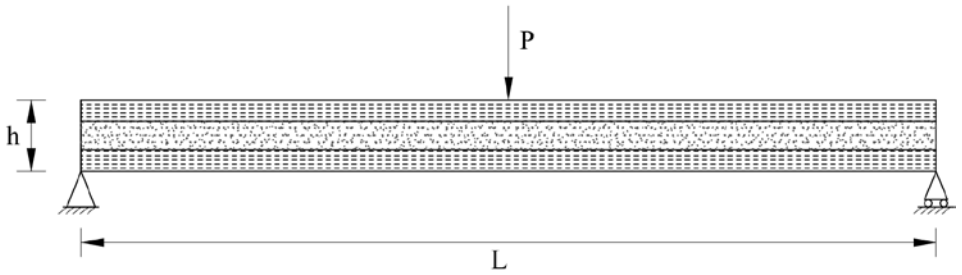
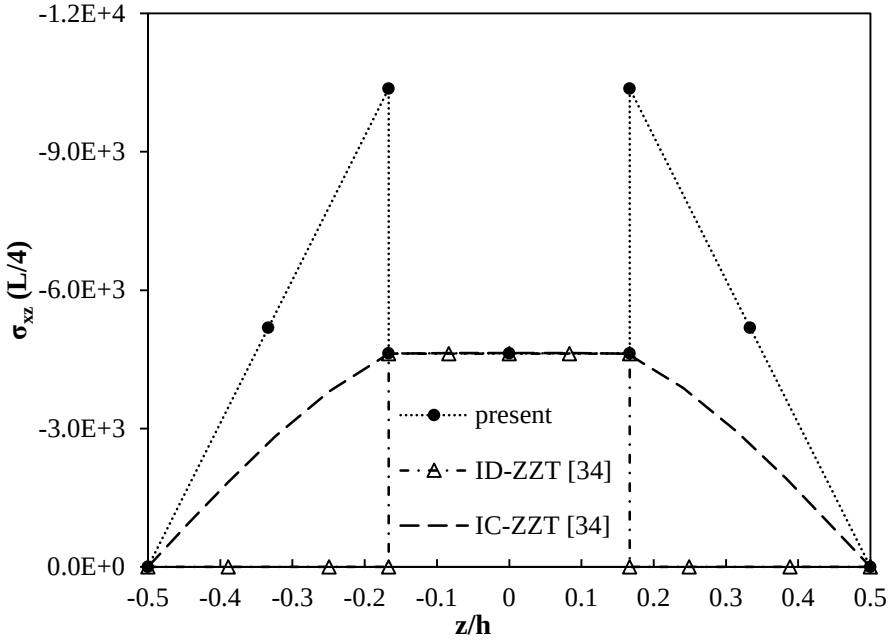
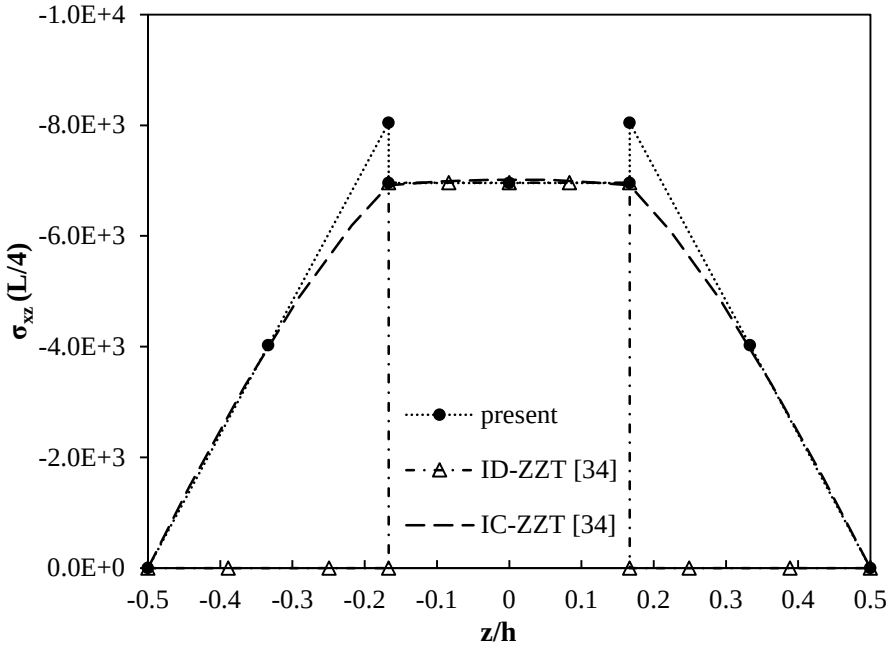


Figure 5: A simply-supported sandwich beam loaded with a transverse force at the midspan.



a. FCSR=10



b. FCSR=10^4

Figure 6: Through-thickness distribution of transverse shear stress $\bar{\sigma}_{xz}$.

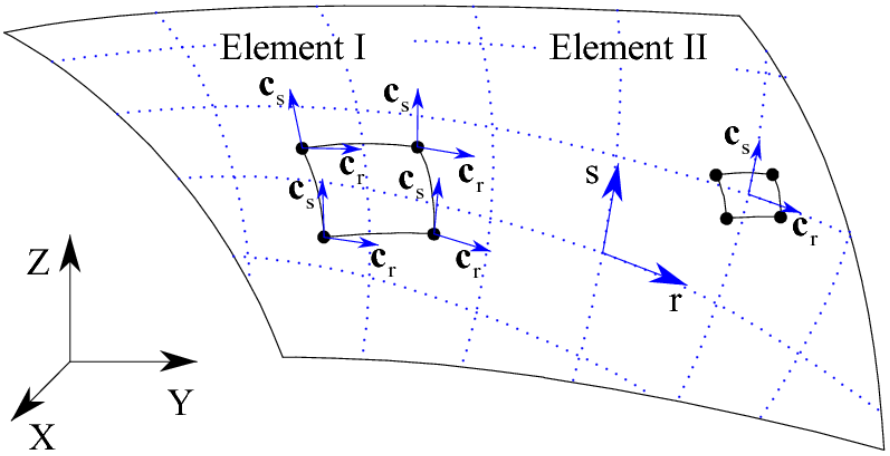


Figure 7: 2D curvilinear shell coordinate system.

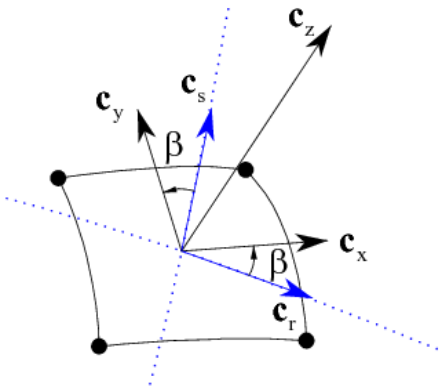
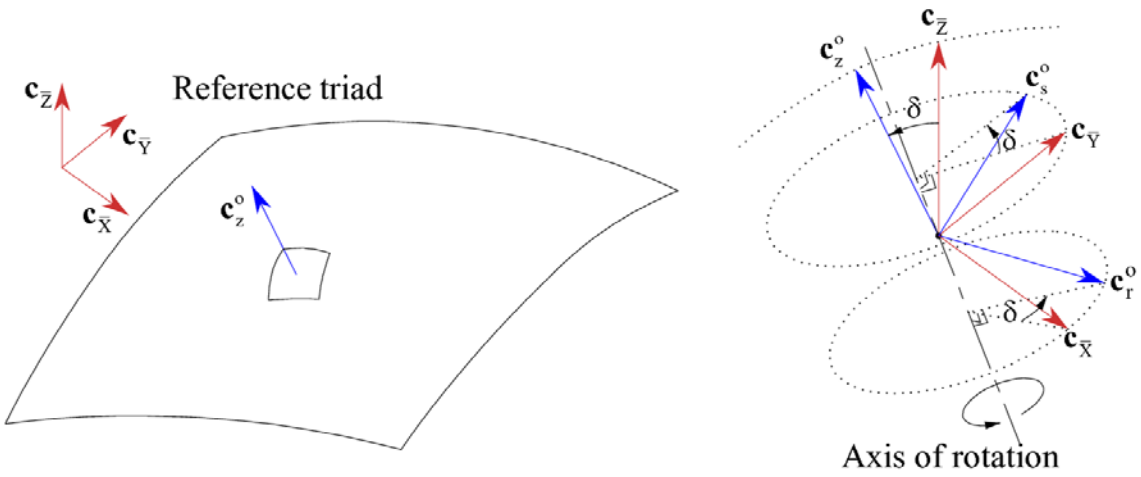
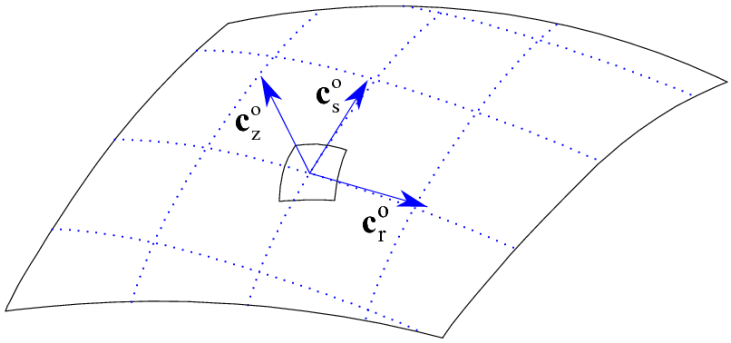


Figure 8: Relative orientation between the local element and shell systems.



a. Rotation of reference triad



b. Resulting curvilinear axes of shell system

Figure 9: An alternative definition of shell coordinate system using a reference triad.

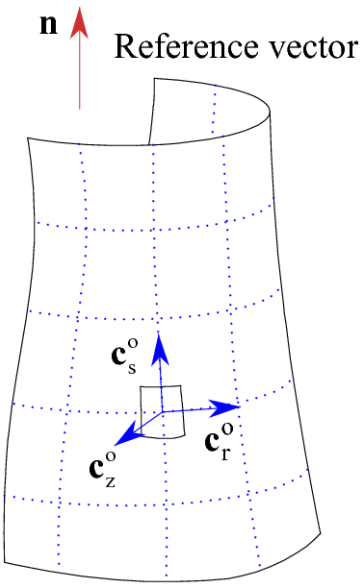


Figure 10: An alternative definition of shell coordinate system using a reference vector.

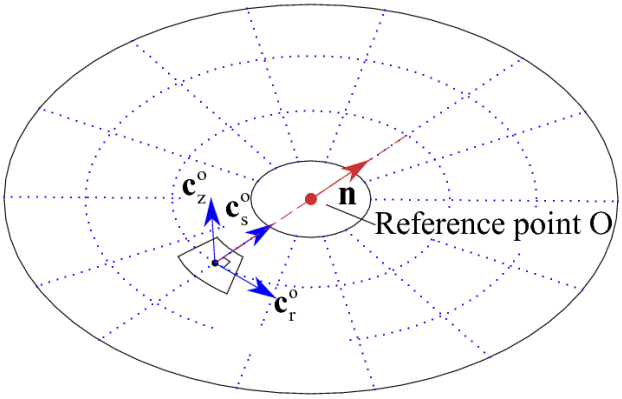


Figure 11: An alternative definition of shell coordinate system using a reference point.

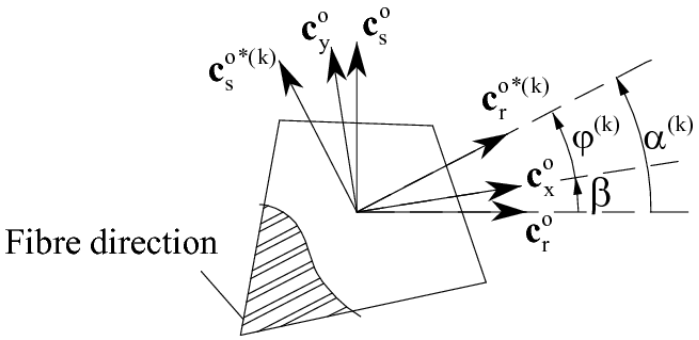


Figure 12: Relative orientation between the local element, the material, and the shell systems.

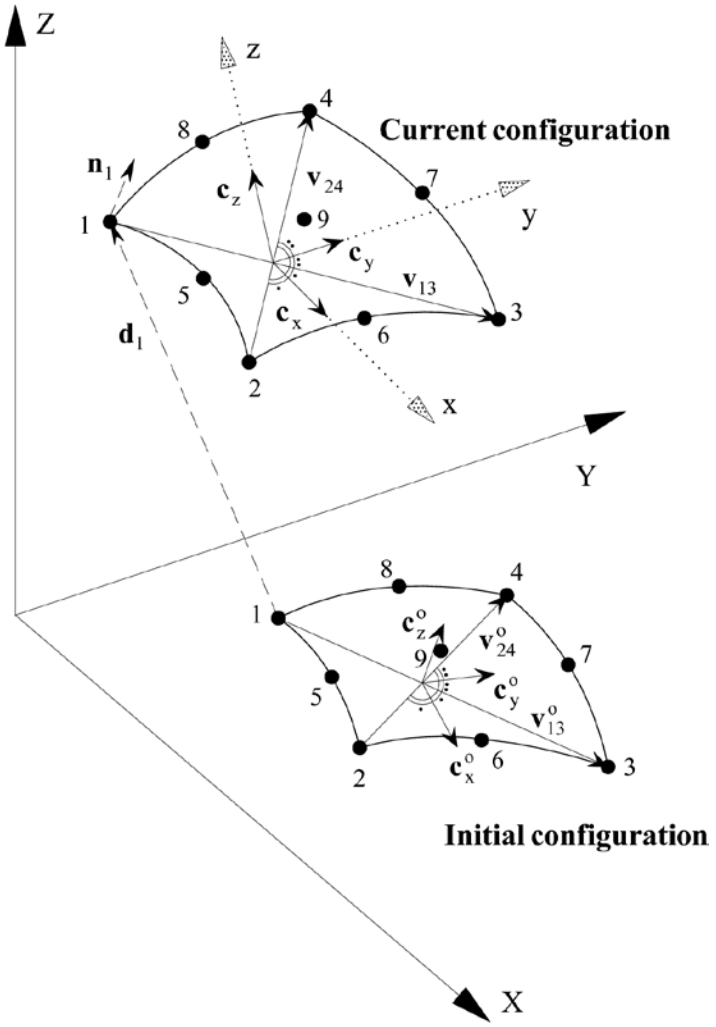


Figure 13: Definition of the bisector co-rotational framework.

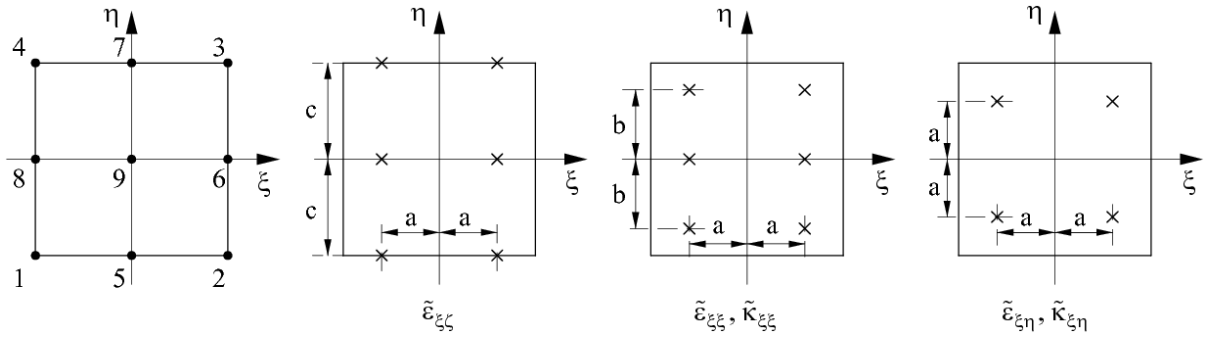


Figure 14: Positions of tying points for MITC9 element ($a = 1/\sqrt{3}$, $b = \sqrt{3/5}$, and $c = 1$).

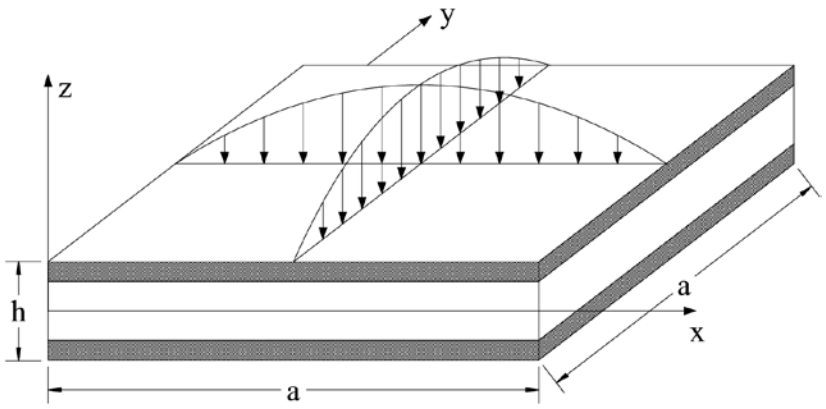
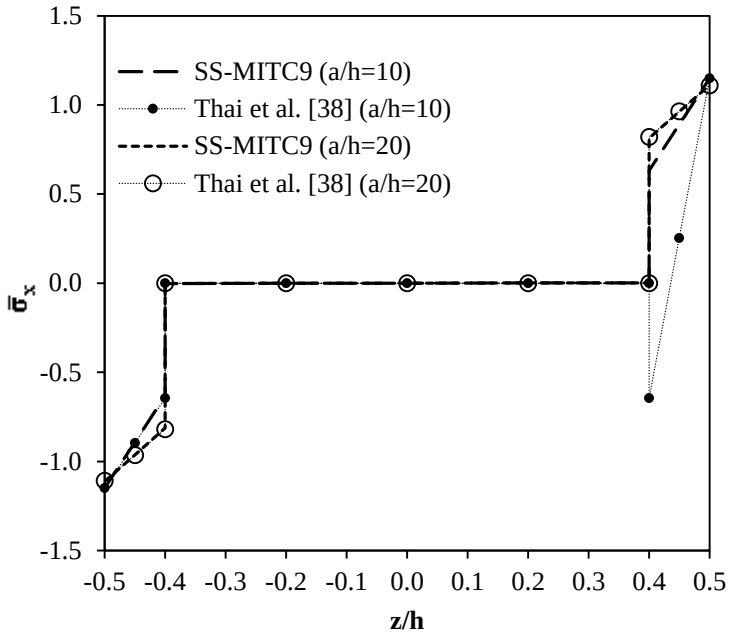
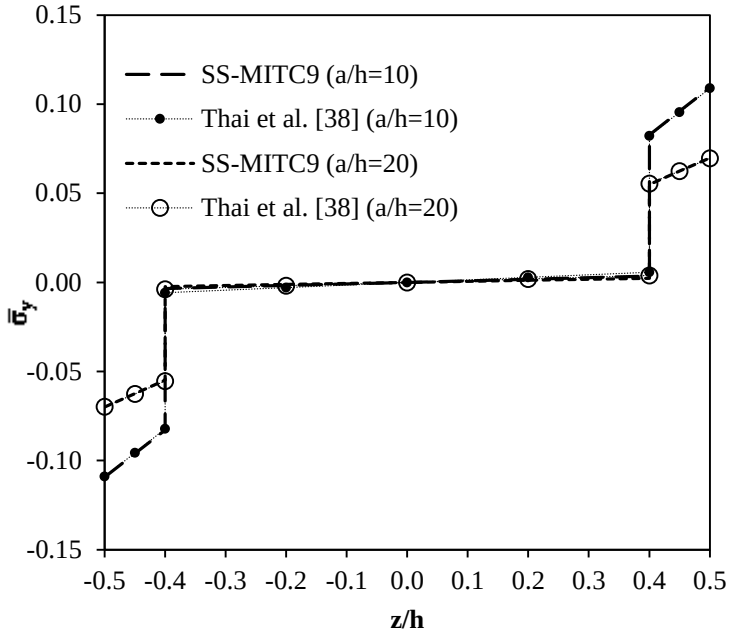


Figure 15: Simply-supported sandwich plate under bidirectional sinusoidal loading.

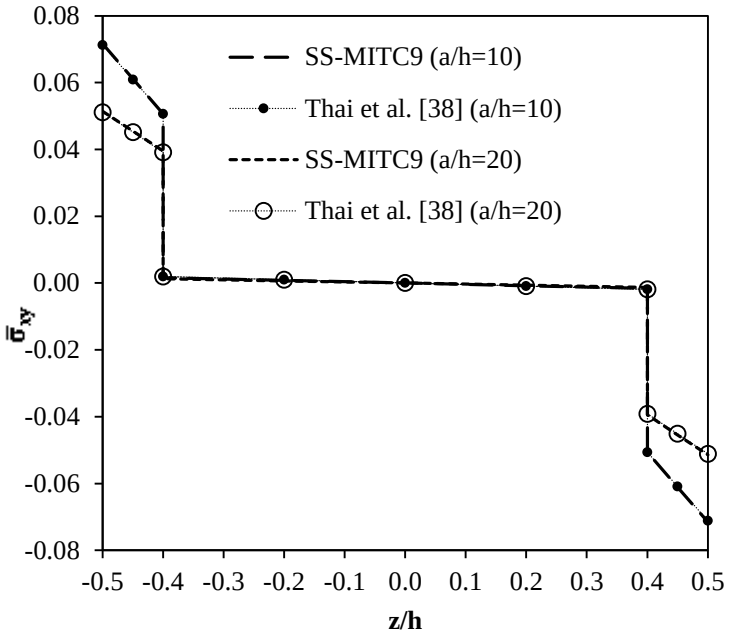


a. through-thickness distribution of $\bar{\sigma}_x$

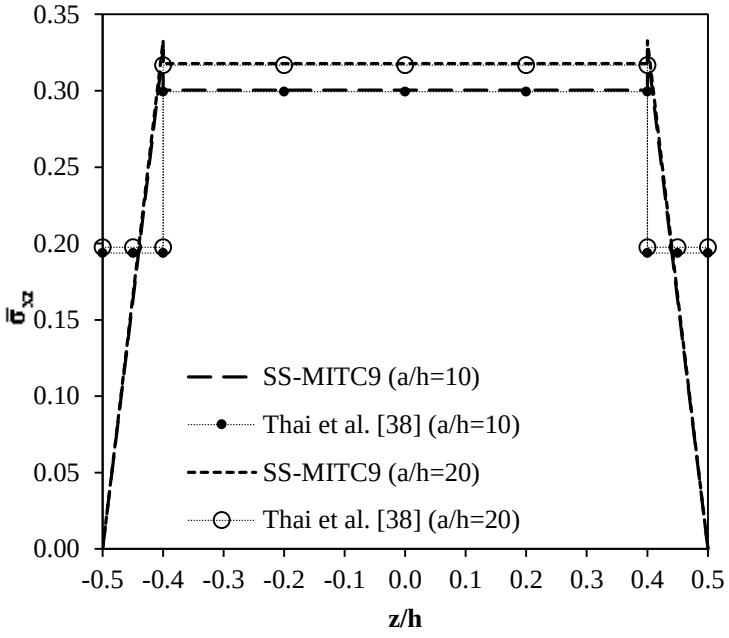


b. through-thickness distribution of $\bar{\sigma}_y$

Figure 16: Through-thickness distribution of non-dimensional stresses for sandwich plate (Cont'd…).

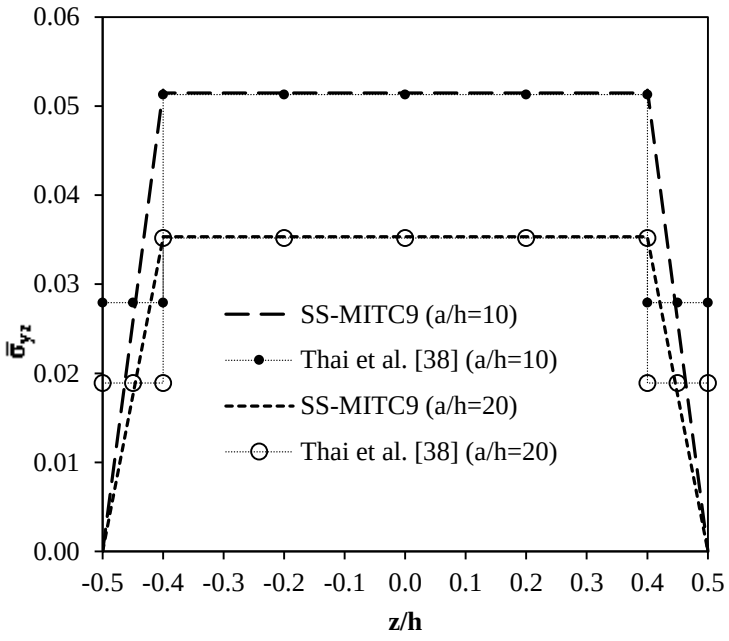


c. through-thickness distribution of $\bar{\sigma}_{xy}$



d. through-thickness distribution of $\bar{\sigma}_{xz}$

Figure 16: Through-thickness distribution of non-dimensional stresses for sandwich plate (Cont'd…).



e. through-thickness distribution of $\bar{\sigma}_{yz}$

Figure 16: Through-thickness distribution of non-dimensional stresses for sandwich plate.

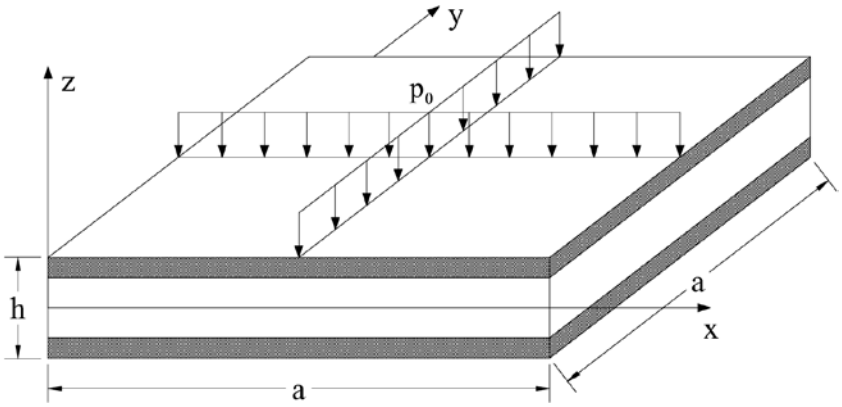


Figure 17: Simply-supported sandwich plate under uniformly distributed loading.

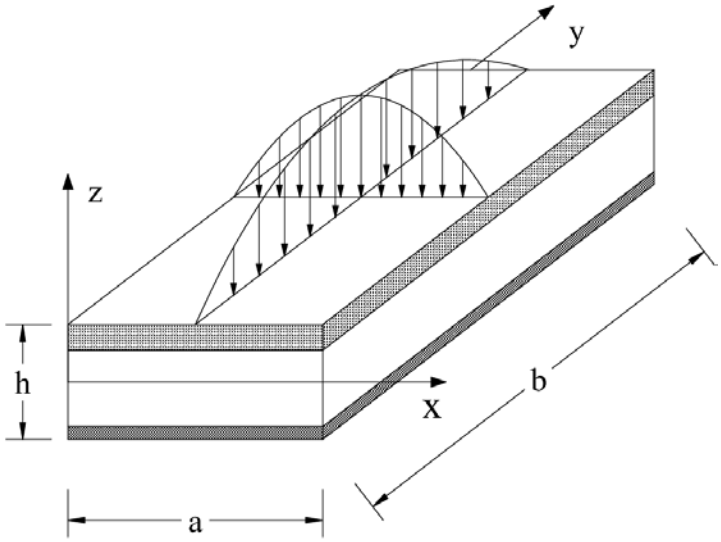
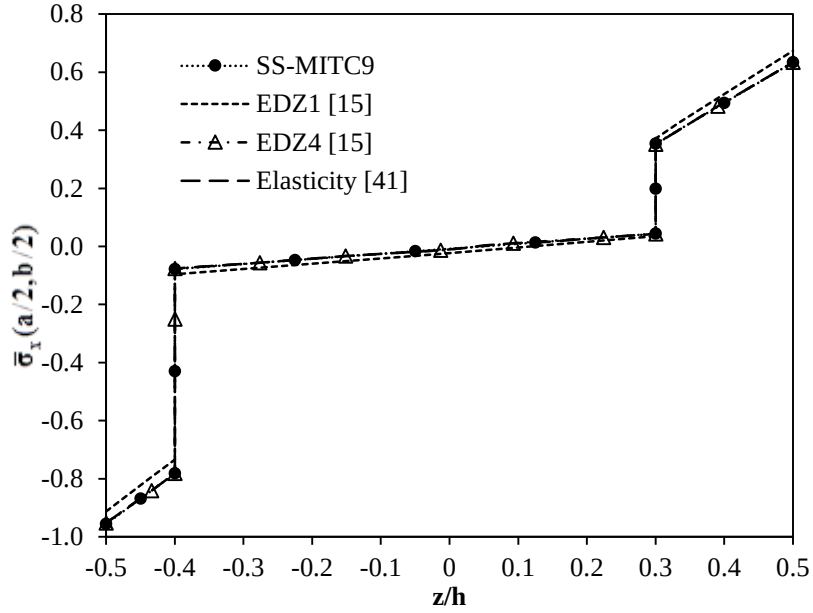
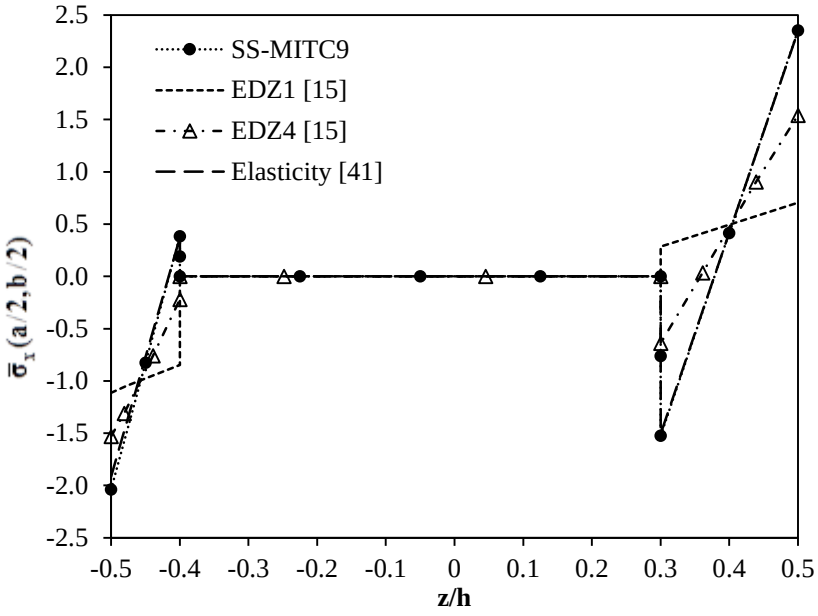


Figure 18: Asymmetrically laminated sandwich plate under bidirectional sinusoidal loading.

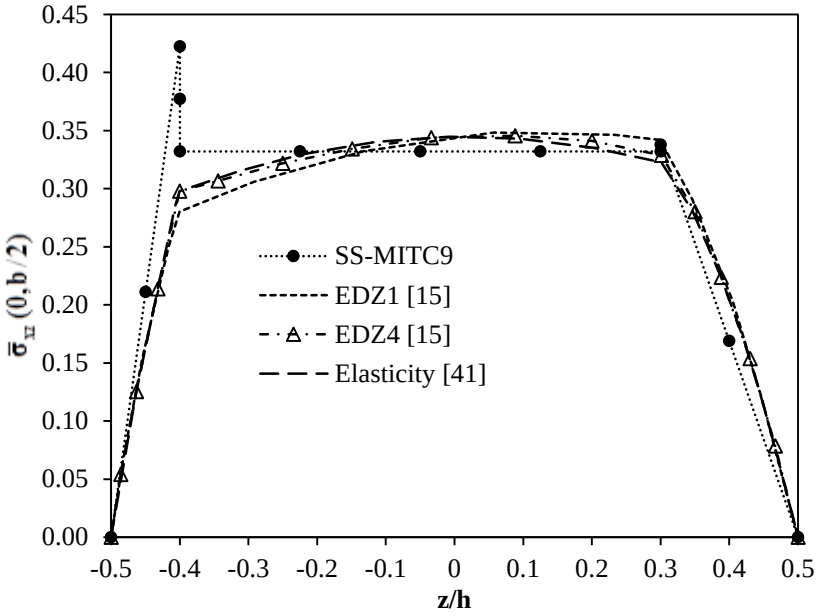


a. FCSR=10, and a/h=100

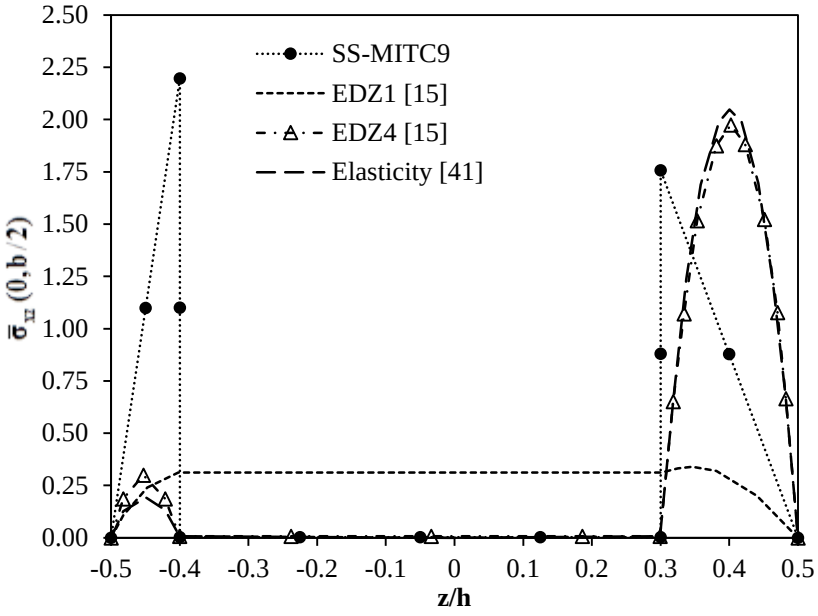


b. FCSR=10^5, and a/h=100

Figure 19: Through-thickness distribution of non-dimensional in-plane stress $\bar{\sigma}_x$.



a. FCSR=10, and a/h=4



b. FCSR=10^5, and a/h=4

Figure 20: Through-thickness distribution of non-dimensional transverse shear stress $\bar{\sigma}_{xz}$.

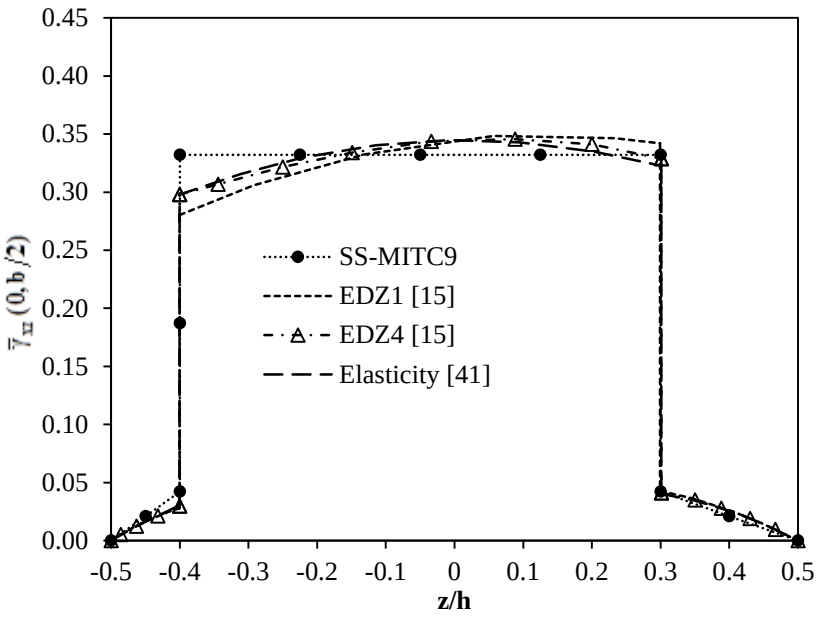


Figure 21: Through-thickness distribution of non-dimensional transverse shear strain $\overline{\gamma}_{xz}$ (FCSR=10, and a/h=4).

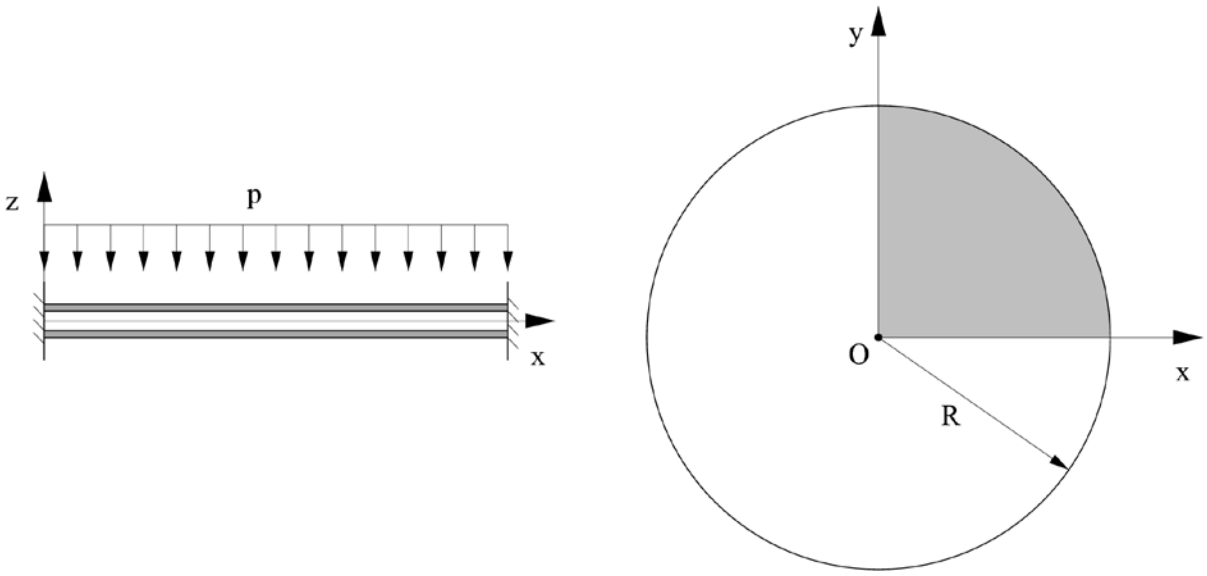


Figure 22: Clamped circular sandwich panel under uniform loading.

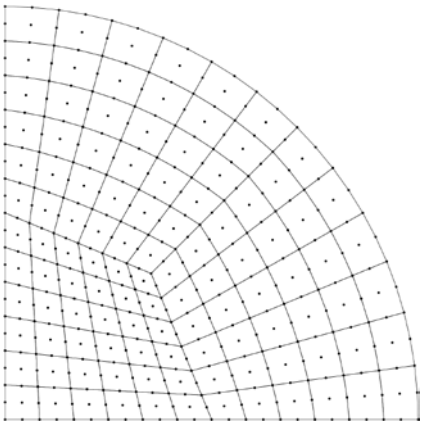


Figure 23: Mesh pattern for a 6×6 mesh of 9-noded sandwich shell elements.

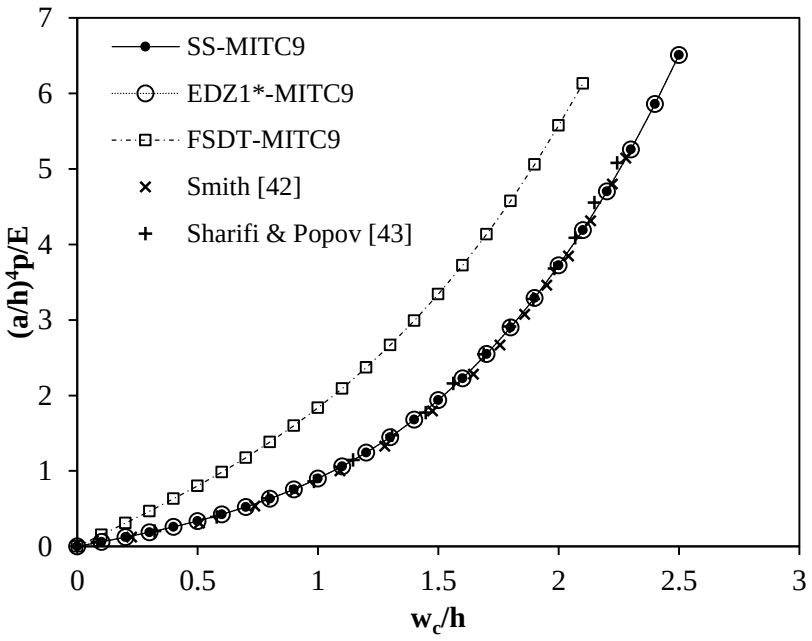


Figure 24: Dimensionless load-deflection curves at point O of various models for a symmetric lay-up.

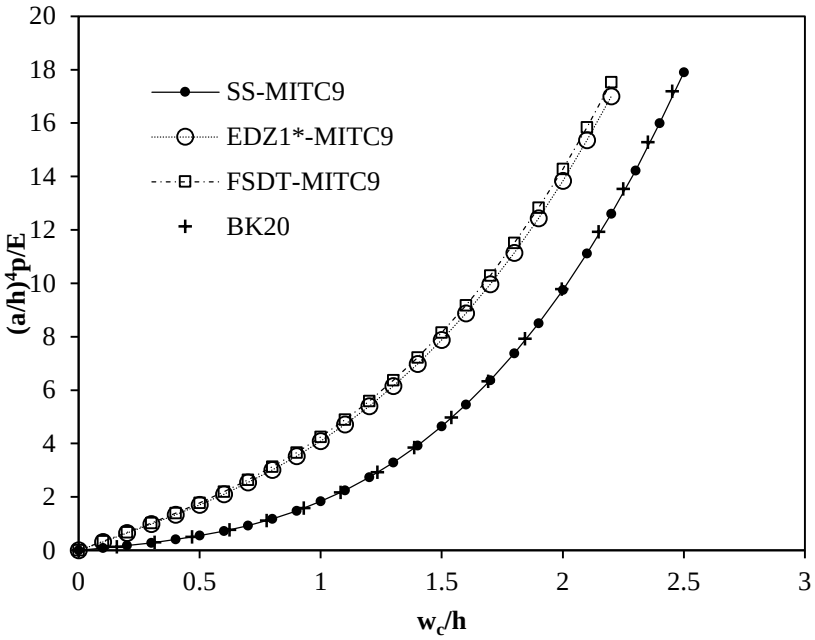


Figure 25: Dimensionless load-deflection curves at point O of various models for an asymmetric lay-up.

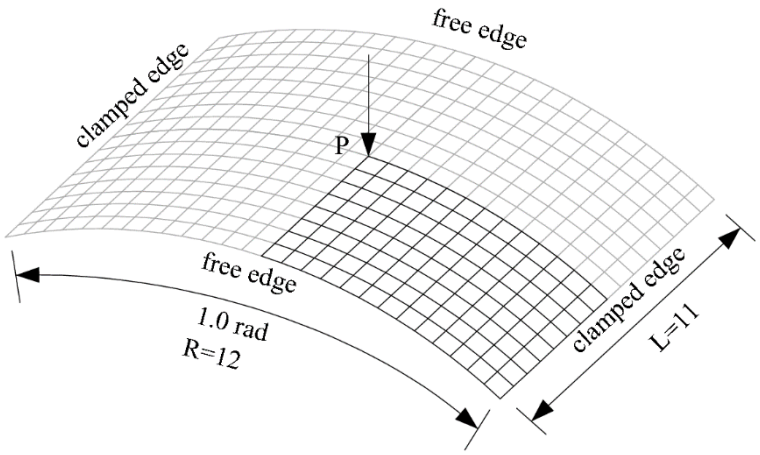


Figure 26: Cylindrical sandwich shell subject to transverse force.

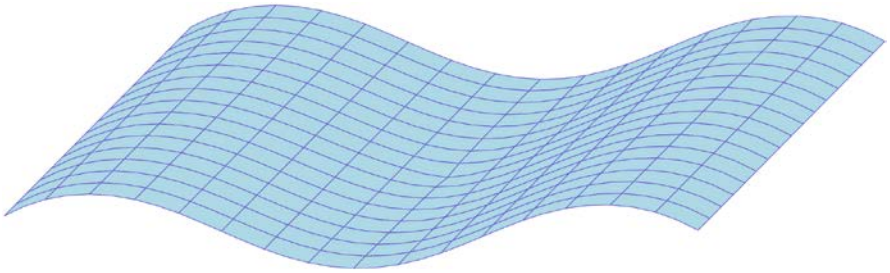


Figure 27: Deflected shape of the transversely loaded cylindrical sandwich shell.

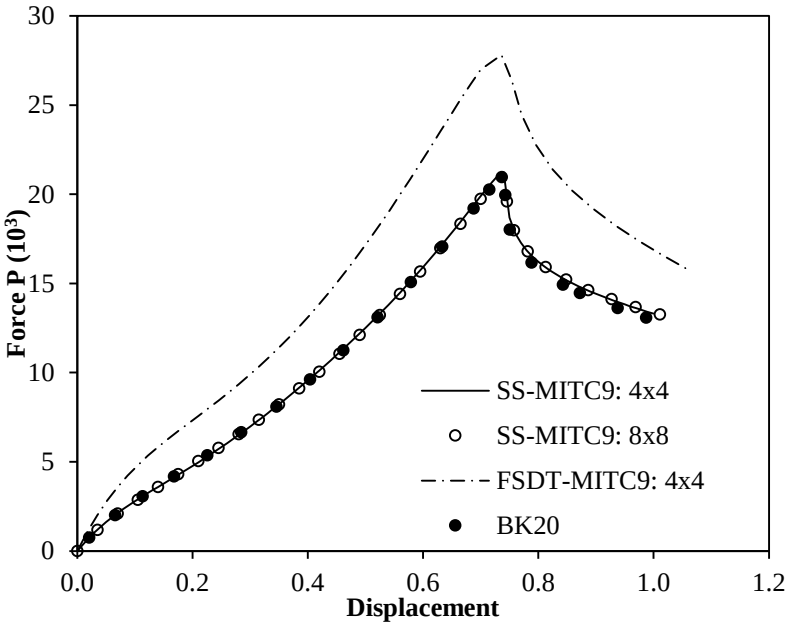


Figure 28: Load-central deflection curves of various models.

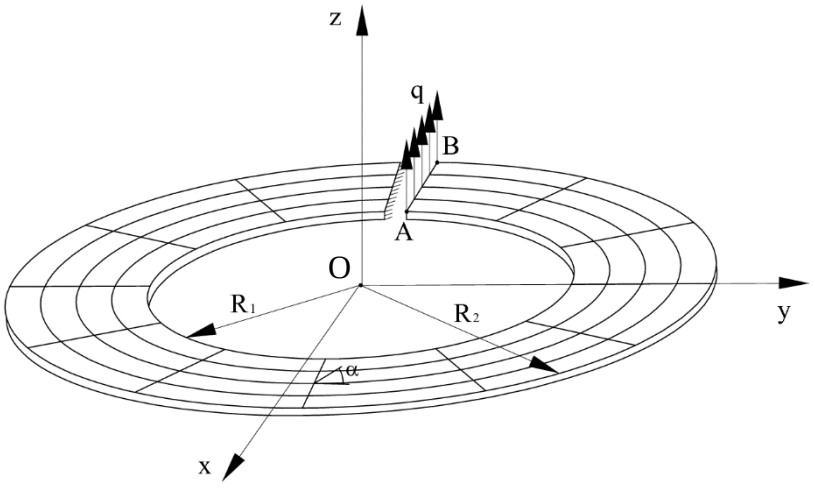


Figure 29: Sandwich annular plate subject to end transverse shear.

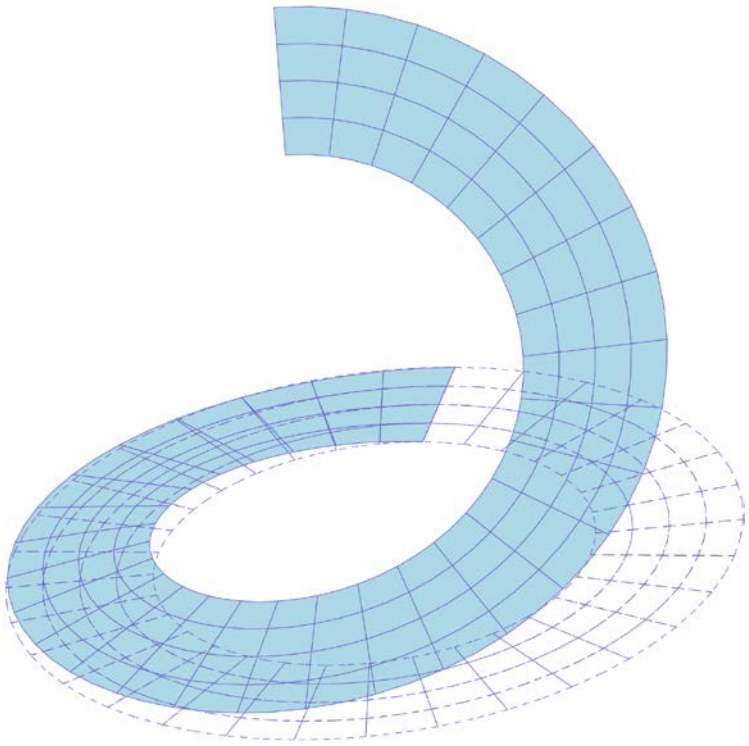


Figure 30: Deflected shape of the annular sandwich plate.

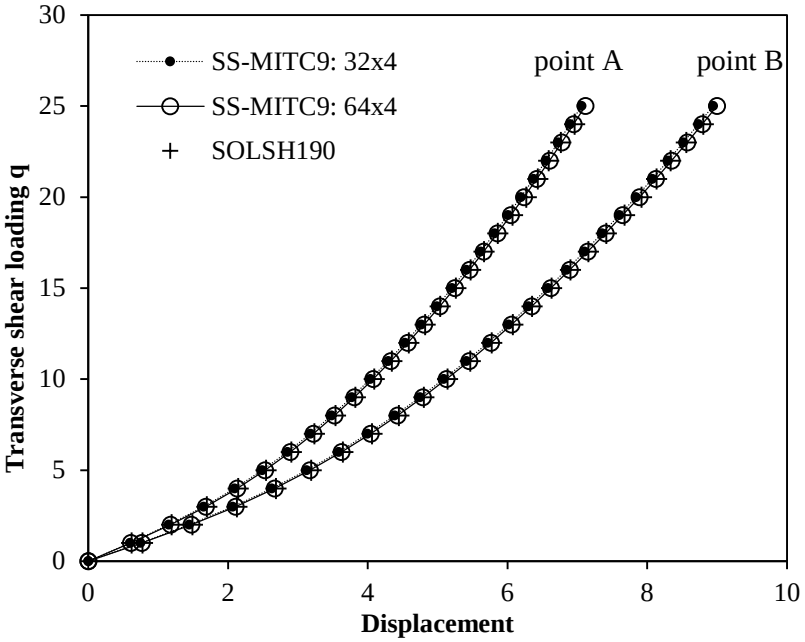


Figure 31: Convergence study along the circumferential direction for SS-MITC9 models

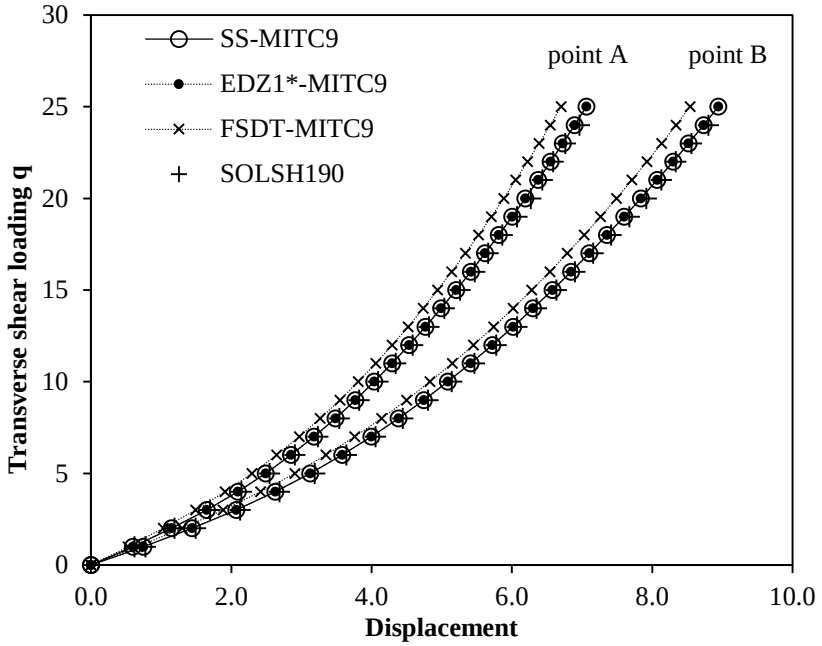


Figure 32: Load-displacement curves of various models for for a symmetric lay-up with a (0°/0°/0°) stacking scheme.

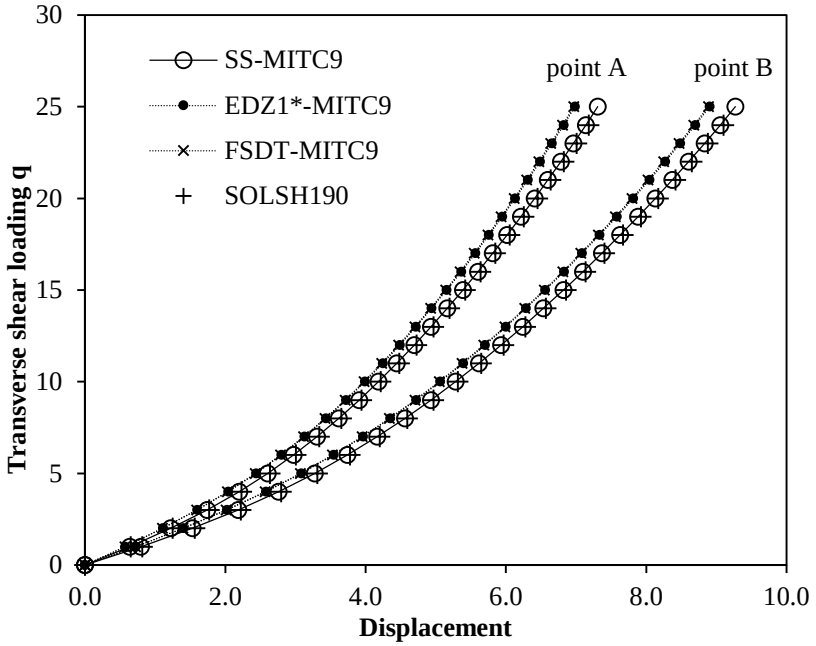
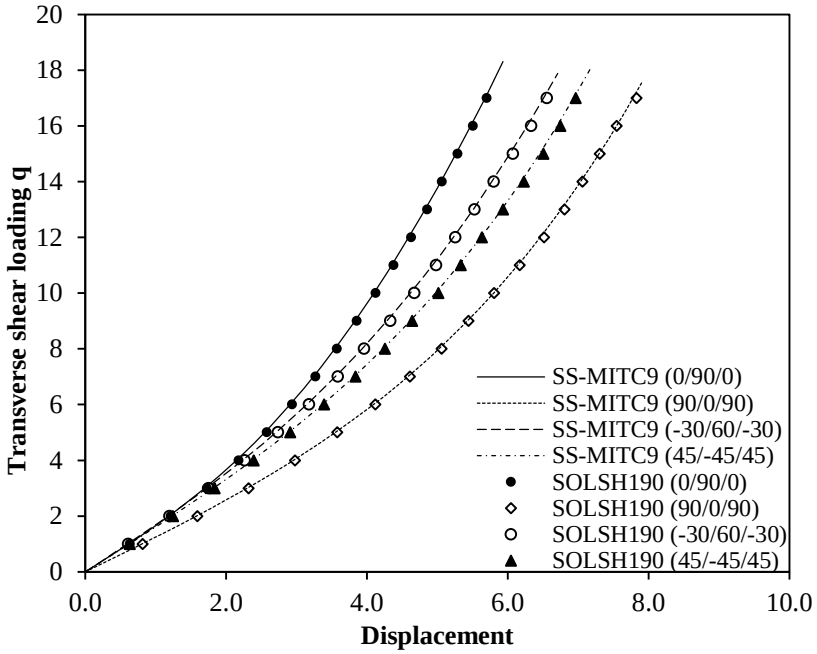
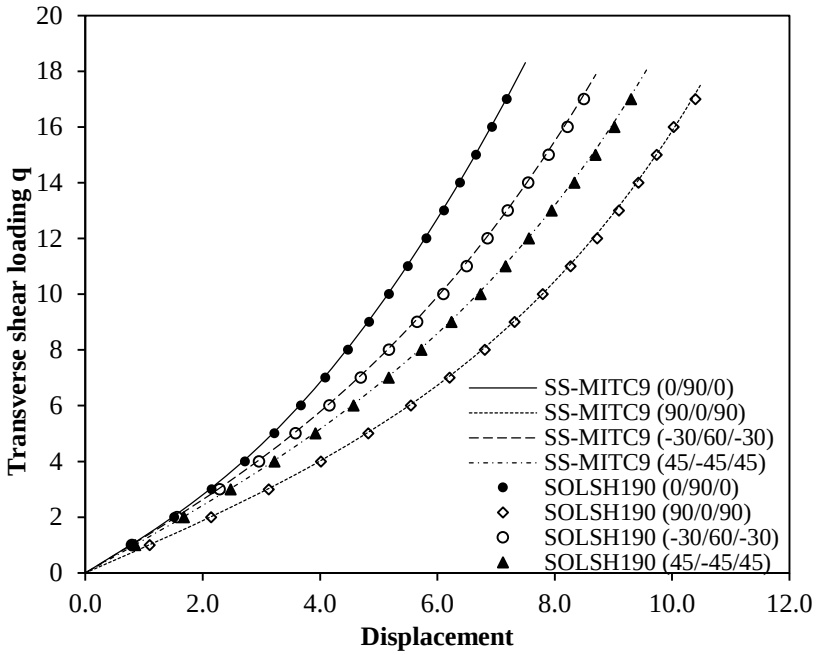


Figure 33: Load-displacement curves of various models for an asymmetric lay-up with a (0°/0°/0°) stacking scheme.



a. point A



b. point B

Figure 34: Load-displacement curves for a symmetric lay-up with various stacking schemes.